PASSIVE RF SENSORS AND WIRELESS SENSOR INTERROGATION

by

SRIKAR DESHMUKH

Presented to the Faculty of the Graduate School of

The University of Texas at Arlington in Partial Fulfillment

of the Requirements

for the Degree of

MASTER OF SCIENCE IN ELECTRICAL ENGINEERING

THE UNIVERSITY OF TEXAS AT ARLINGTON

August 2010

Copyright © by SRIKAR DESHMUKH 2010

All Rights Reserved

To my parents, brother, sister-in-law and

my Late uncle Deshmukh Jagannatha Rao.

Knowledge is something that cannot be stolen by a thief or snatched by a King,

it is not something that can be divided among siblings,

it is never a burden to carry around, it only increases on spending.

Thus, the wealth of knowledge is the greatest of all possessions.

- Subhashitam

ACKNOWLEDGEMENTS

I am grateful to my research advisor, Dr. Haiying Huang, who has been my guide, inspiration and support throughout my course work. She has been my role model since the time I started my research under her guidance and I could not have achieved much without her moral and financial support. I am also thankful to Dr. Mingyu Lu, for all his encouragement and support. I am grateful to Dr. Saibun Tjuatja for supporting me and agreeing to be a part of my thesis committee.

I am indebted to my family, my Mother Purnima, my Father Muralidhar, my Brother Srikanth and my Sister-in-law Divya for believing in me and encouraging me. My Father's encouragement, from the first time I rigged up simple electronic circuits (when I was in class 3) to this day, has been a huge source of motivation. Thank you Dad!!

I would like to thank my friends, Swanand, Rakesh, Vinay, Cheeku and Moose, for their moral support and encouragement. Finally, I would like to thank Irshad, Manjunath, Deniz, Jensen, Ye and Justin for the memorable time we have had in our lab.

May 28, 2010

ABSTRACT

PASSIVE RF SENSORS AND WIRELESS SENSOR INTERROGATION

SRIKAR DESHMUKH, M.S.

The University of Texas at Arlington, 2010

Supervising Professor: Haiying Huang

Recently, a new type of passive sensor called the antenna sensor has been developed. The antenna sensor incorporates a patch antenna as the sensing element as well as the data transmitting element. Physical factors such as strain and ground plane crack cause the patch antenna resonant frequency to change. By measuring the change in patch antenna resonant frequency these physical factors can be quantified.

Conventional resonant frequency measurement methods require a wired connection to the antenna sensor. The wireless interrogation technique eliminates this requirement while offering all the advantages that a wireless sensor interface offers over a wired sensor interface. In this technique, a wideband interrogation signal is transmitted towards the antenna sensor. The backscatter signal, comprising of antenna mode and structure mode, is normalized to isolate the antenna mode backscatter from which antenna sensor resonant frequencies can be extracted.

The concept of backscatter normalization, implementation of the normalization scheme and interrogation characteristics are described. In addition, preliminary study on using other microwave components, such as ring resonator, for crack and strain measurement is also presented.

TABLE OF CONTENTS

LIST OF FIGURES

CHAPTER 1

INTRODUCTION

1.1 Introduction

Structural Health Monitoring (SHM) is the process of detecting and monitoring structural damages [10][32][29][8]. All structures undergo a process of damage and deterioration over a period of time and extreme changes in operational environment can accelerate this process. Thus, it is of utmost importance to monitor the structural health of civil and aerospace structures to improve their reliability. SHM is especially important for those structures that are operating beyond their designed service life. SHM involves observation of the structure using one or more distributed sensors monitoring one or more properties of the structure. Some of the important properties that are used to quantify the health of a structure are fatigue cracks, strain, temperature and displacement. The main components of a typical SHM system are listed below.

1. Structure
2. SHM sensors
3. Sensor interface and network management
4. Sensor data processing
5. Sensor data interpreter and data management
6. Service life estimation

1.2 Sensors for SHM

1.2.1 Types of SHM sensors

Based on their interfacing methods SHM sensors can be categorized as wired and wireless sensors. Wired SHM sensors are typically robust and cost less than the wireless SHM sensors. Wireless SHM sensors enable dense sensor deployment, easy installation and reconfiguration and can be efficiently networked in applications where sensor wiring is not possible.

Based on the power source, SHM sensors can either be passive or active. Active sensors have a dedicated power source incorporated within the sensor. The power source usually contributes a large part to the weight of these sensors. Moreover, in the case of wireless sensors, the usage of battery as the power source limits the life span of the wireless sensor nodes. The passive sensors harvest energy from ambient energy sources such as mechanical vibrations, temperature gradient, optical power, etc. Passive sensors have long operational life, low maintenance and a compact form factor. The energy from ambient sources is generally low and the harvesting process in passive sensors requires considerable amount of time to gather enough energy for normal operation. This inherent characteristic of passive sensors limit their ability to measure in real time.The most common passive wireless sensors are based on radio frequency identification (RFID) concept and surface acoustic wave (SAW) devices [1][24][36]. This type of sensor uses a RFID tag to receive an interrogation signal from the reader while the SAW device converts the received electrical signal into surface wave used to perform measurement. The surface wave is then converted back into electrical signal and transmitted back to the reader using the same RFID tag. The double conversion process results in low efficiency and short range. Passive wireless sensors have also used induction coupling for power and data transmission [5][13][15].

In this type of passive wireless sensor, a parallel LC tank circuit is connected to a coil. The measurand changes either the inductance or the capacitance of the LC tank circuit, thus changing its resonant frequency. The reader coil magnetically couples to the sensor coil in order to induce energy into the sensor circuit and perform the measurement. This magnetic coupling results in high losses and consequently very low range, of the order of a few centimeters.

1.2.2 Sensing technologies

A large number of sensing technologies have been developed to cater the wide range of SHM monitoring applications. Changes in structural strain fields and fatigue cracks are two important properties that are measured by SHM sensors to quantify the structural health. Fiber Bragg sensors use a distributed Bragg reflector in an optical fiber to obtain wavelength filters that are sensitive to the grating period [28][31]. When embedded in composite structures or when mounted on conventional structures, changes in structural strain distribution changes the grating period causing a change in the filter wavelength. Thus, by periodically measuring the filter wavelength, strain distribution and hence the structural health can be monitored. Alternatively, conventional meandering-line strain sensors could be used to measure changes in strain distribution. The strain sensors can also indirectly measure fatigue cracks since the fatigue cracks change the strain distribution on a structure. Other sensing technologies directly monitor fatigue crack growth to accomplish the task of SHM. Acoustic Emission (AE) sensors passively monitor the acoustic signal emissions due to structural damage [14]. Ultrasound sensors actively transmit an ultrasound wave in the structure and study the received signal across the area of interest. Cracks in the structure change the structural response to the ultrasound wave. This change in structural response is very small and is challenging to isolate from other noises and

interference sources. It is also difficult to accurately decipher the location and size of cracks on a structure using ultrasound sensors [30][40][35].

1.3 Antenna sensor for SHM applications

Of late, a new type of passive wireless sensor has been developed [34]. This SHM sensor, called the antenna sensor, utilizes a patch antenna for sensing as well as transmitting the measurement data. The antenna sensor can be used to measure both strain and fatigue cracks in the structure to quantify its structural health. It is light weight, low cost, low profile, requires negligible power for its operation and is conformable to most structural surfaces. A large number of antenna sensors can be multiplexed in frequency domain to build large scale sensor networks with dense sensor deployment. The antenna sensor is highly sensitive to strain and fatigue crack propagation [34][21]. Figure 1.1 shows a typical antenna sensor mounted on a Compact Tension specimen.

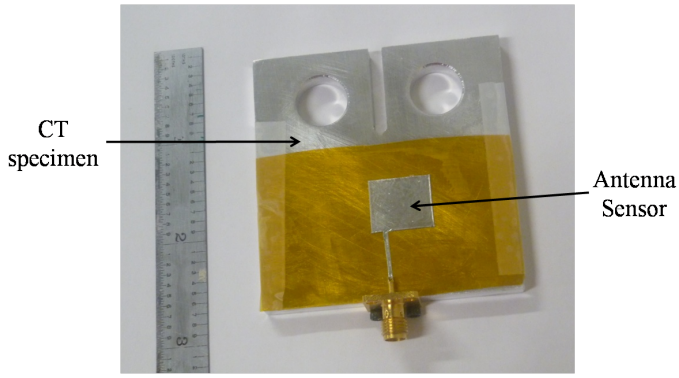

Figure 1.1. Typical antenna sensor mounted on a CT specimen.

A patch antenna can have two resonant frequencies f_{01} and f_{10} corresponding to the two dominant modes TM_{001} and TM_{010}. The resonant frequencies of TM_{10} and TM_{01} modes are sensitive to the width and length dimensions of the patch antenna

respectively. Strain acting on the patch antenna changes its dimensions, thus changing its resonant frequencies [34]. In order to measure strain changes in a structure, the patch antenna is bonded securely to the structure. By monitoring for changes in patch antenna resonant frequencies, it is possible to quantify changes in the structural strain.

It has also been found that cracks in the ground plane of a patch antenna change the ground plane current distribution, thus changing its resonant frequencies. This phenomenon can be used to detect fatigue cracks in metallic structures. The structure of interest can be used as the ground plane for the patch antenna. When fatigue cracks form in the structure under the patch antenna, its resonant frequencies change. This phenomenon has also been applied in telecommunication equipments to design patch antennas with switchable resonant frequencies [6].

The resonant frequency of individual patch antenna modes are sensitive to strain along their corresponding dimensions. Similarly, the resonant frequency of individual patch antenna modes are sensitive to ground plane crack propagation perpendicular to their corresponding dimensions. This characteristic of antenna sensor makes it suitable for measuring both the magnitude and direction of strain or structural cracks.

Antenna sensor resonant frequency can be determined by measuring its S_{11} parameter. In the S_{11} parameter plot over frequency, antenna sensor resonant frequency can be identified as the frequency at which its return loss is minimum. Measuring the S_{11} plot of an antenna sensor requires a physical connection to the patch antenna using one of the many coupling methods like microstrip line, coaxial probe, aperture coupling and proximity coupling [3][2][7][19][25].

1.4 Wireless interrogation using backscattering technique

1.4.1 Concept of backscattering

The antenna sensor can be interrogated wirelessly by using the concept of backscattering. When a wideband interrogation signal is incident on the antenna sensor, a part of the interrogation signal whose frequency matches with the resonant frequency of the antenna sensor is received by the antenna sensor. If the antenna sensor is not terminated with a matched load, the received signal gets reflected at the mismatched load and gets re-radiated. This re-radiated signal, called the antenna mode backscatter, has a dominant signal of frequency equal to the resonant frequency of the antenna sensor. Thus, by observing the frequency components of the antenna mode backscatter it is possible to wirelessly measure the antenna sensor resonant frequency.

1.4.2 Issues using backscattering based remote interrogation

When the antenna sensor is exposed to a wideband interrogation signal, in addition to the antenna mode backscattering, the structures surrounding the antenna sensor scatter back the interrogation signal, creating the structural mode backscatter. The structural mode backscatter dominates the antenna mode backscatter since it is typically one or two orders of magnitude greater than the antenna mode backscatter. Thus, without canceling the structural mode from the backscattered signal, it is not possible to determine the antenna sensor resonant frequency.

1.4.3 Backscatter normalization technique

The antenna mode backscatter can be isolated from the structural mode backscatter using an impedance switching based normalization technique. In this technique, two backscatter measurements are taken, one with the antenna sensor connected to

an open circuit termination and another with the antenna sensor connected to a short circuit termination. Since the surrounding structure remains the same for these two measurements, the structural mode backscatter signal is assumed to be constant. The change in termination impedance of the antenna sensor from open circuit to short circuit causes the antenna mode backscatter in the second measurement to shift its phase by 180° with respect to the first measurement. Thus, by subtracting these two measurements, the structural mode backscatter gets canceled while the antenna mode backscatter gets doubled.

1.5 Ring resonator based crack sensor and strain sensor

A microstrip ring resonator is a microstrip transmission line based resonator, typically consisting of a closed ring of transmission line. When energy is coupled into the ring, a standing wave is generated across the ring, resonating at a frequency determined by the circumference of the ring and the relative dielectric constant of substrate below the microstrip ring.

When the ring resonator is bonded to a structure, it flexes when exposed to structural strain. This causes the circumference of the ring to change, therefore changing its resonant frequency. Thus it is possible to measure strain by measuring the ring resonant frequency. Also, it has been shown that if the symmetry of the ring in the ring resonator is disturbed, two degenerate modes can be excited in the ring resonator [37]. Ring symmetry can be disturbed by a crack in one of the arms of the ring. The resonant frequency of degenerate mode can be correlated to the length of the crack. Thus it is possible to measure crack in the structure by bonding a ring resonator to it and measuring the ring resonant frequencies.

Since the ring resonator requires negligible power to operate, has a low profile and can be easily multiplexed in frequency domain, it is well suited for sensing

applications that require strain or crack sensing capability in inaccessible areas of the structure. The ring resonator can also be interfaced with wireless interrogation scheme to offer the wireless interrogation capability.

1.6 Thesis Overview

Wireless interrogation is an important feature required to network large number of antenna sensors offering dense sensor deployment. This feature enables remote measurement of antenna sensor resonant frequencies without requiring a dedicated power source on the antenna sensor. The wireless interrogation scheme transmits a wideband interrogation signal towards the antenna sensor and processes the backscatter signal to recover the resonant frequencies of antenna sensor. An impedance switching based backscatter normalization scheme is used to cancel the background signal clutter while isolating the backscatter signal from the antenna sensor.

The principle of operation of the impedance switching based backscatter normalization scheme, its implementation and tests to verify the wireless interrogation characteristics are presented. Two innovative applications of ring resonator are also presented along with numerical simulation verifying their proof-of-concepts. More specifically,

- Chapter 2 describes the contact-based methods of measuring the antenna sensor resonant frequency.
- Chapter 3 presents the concept of backscattering and impedance switching based backscattering normalization technique for isolating the antenna mode backscatter. An experiment is described to evaluate a microwave switching circuit used to switch the impedance of an antenna sensor. The final implementation of the backscatter normalization circuit is also explained.

- Chapter 4 discusses the signal processing algorithm and experimental setup used to interrogate antenna sensor. A detailed analysis of the power budget model for the wireless interrogation is described. Experimental setup for characterizing the angular response of the remote interrogation scheme is also described.
- Chapter 5 proposes the application of microstrip ring resonator as a crack sensor and as a strain sensor. Numerical simulations and description of the ring resonator's responses to crack and strain are presented.
- Chapter 6 discusses the measurement results for the antenna sensor angular response test and the microwave switching circuit evaluation described in chapter 3. The measurement results obtained using remote interrogation setup described in chapter 4 are presented. Simulation results for the microstrip ring resonator models described in chapter 5 are also presented.
- Chapter 7 summarizes the conclusions and presents the future work.

CHAPTER 2

CONTACT METHOD OF ANTENNA SENSOR INTERROGATION

2.1 Introduction

The antenna sensor resonant frequencies vary as a function of strain and ground plane crack propagation. Thus, the strain or crack measurement information from an antenna sensor can be read by measuring its resonant frequencies. Resonant frequencies can be measured by exciting the dominant modes of the antenna sensor and measuring the frequency of these dominant modes. The excitation can be achieved by using a feed line coupled to the antenna sensor.

The different methods of antenna sensor - feed line coupling and types of contact-based methods of resonant frequency measurement are explained in this chapter.

2.2 Antenna sensor coupling methods

Typical coupling schemes used to couple antenna sensors are inset-fed coupling, edge-fed coupling, aperture coupling and probe-fed coupling. Depending on the application each of the coupling schemes have their own advantages and disadvantages. The aperture coupling, though complicated in construction, provides a robust method of coupling an antenna sensor without disturbing its radiation pattern or generating probe self reactances [26]. Inset-fed coupling provides a good impedance match and is simple to construct. Edge-fed coupling is also easy to construct and offers good impedance matching when combined with other impedance matching techniques. Both edge-fed coupling and inset-fed coupling change the radiation pattern

of the antenna sensor and cause self reactances in the feed line [26]. Edge feed and inset feed coupling can be used with gap coupler to reduce the impact of feed line on the antenna sensor [18].

2.3 Contact method of resonant frequency measurement

The contact method of resonant frequency measurement realizes the antenna sensor as a wired sensor requiring, at a minimum, an electrical cable from the measurement system to the antenna sensor. Depending on the measurement setup, the contact method of resonant frequency measurement can be implemented by measuring either the reflection parameter of the antenna sensor or the transmission parameter of the antenna sensor. The transmission parameter measurement method is more complicated to setup compared to the reflectance parameter measurement method but it provides more information about the dominant modes in the antenna sensor than the latter.

2.3.1 Reflectance parameter measurement

The resonant frequency of the antenna sensor can be measured by observing its S_{11} parameter. The resonant frequencies are frequencies at which the antenna sensor S_{11} parameter plot shows distinctive dip, indicating low VSWR at those frequencies. Typical experiment setup for measuring the antenna sensor resonant frequency using the reflectance parameter measurement method is shown in Figure 2.1. In the experiment setup, the antenna sensor is connected to a Vector Network Analyzer (VNA) to measure the S_{11} parameter over the desired frequency range. Though simple to setup, the reflectance parameter measurement method does not relate the resonant frequencies with their corresponding dominant modes of the antenna sensor. It is not

possible to know the resonant frequency along a particular dimension of the antenna sensor using this method.

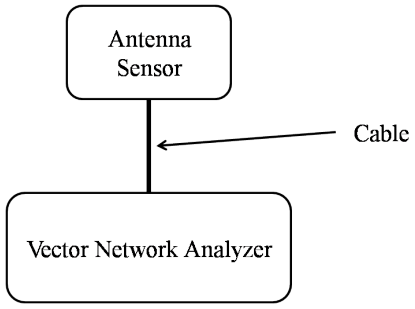

Figure 2.1. Reflectance parameter measurement setup.

2.3.2 Transmission parameter measurement

The typical experimental setup used to measure the antenna sensor resonant frequency using transmission parameter measurement method is shown in Figure 2.2. A wideband antenna is connected to one of the VNA ports and the antenna sensor is connected to another port. The antenna sensor is then placed in the far field of wideband antenna. The VNA is configured to measure S_{12} transmission parameter over the desired frequency range. Since the experiment setup is a reciprocal two-port network, the S_{21} parameter can also be measured instead of S_{12} parameter. The antenna sensor resonant frequencies can be identified by observing the transmission parameter plot. The transmission loss will be minimum at the antenna sensor resonant frequencies. The resonant frequency of individual dominant modes of the antenna sensor can be measured by aligning the wideband antenna polarization along their corresponding dimensions of the antenna sensor. The transmission parameter measurement method can be extended to measure the gain of an antenna sensor using three-antenna method [16].

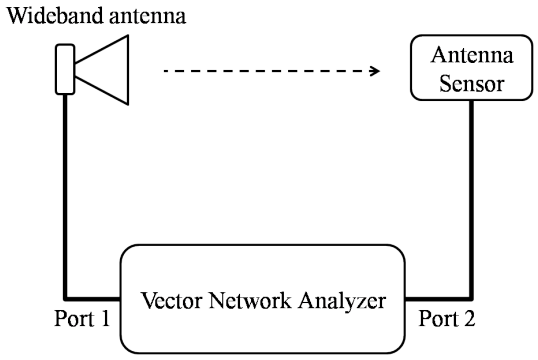

Figure 2.2. Transmission parameter measurement setup.

2.4 Summary

Antenna sensor resonant frequencies can be measured by using two types of contact methods, reflectance parameter measurement method and transmission parameter measurement method. While the reflectance parameter measurement method is simple to setup, the transmission parameter measurement method can be used to measure resonant frequencies of individual dominant modes in the antenna sensor.

CHAPTER 3

BACKSCATTER NORMALIZATION TECHNIQUE

3.1 Introduction

Being an antenna by itself, the antenna sensor can be remotely interrogated without an electrical cable. Measuring the resonant frequencies of the antenna sensor by non-contact means is similar to that done by contact means, except that the excitation source and measurement interface of antenna sensor dominant modes are wirelessly connected. Non-contact antenna sensor interrogation method eliminates the practical limitation on the maximum number of antenna sensors that can be networked while offering flexibility in configuring multiple antenna sensors.

The concept of backscattering, as applied to antenna sensors, is explained in this chapter. An impedance switching based backscattering normalization scheme and its implementation are described.

3.2 Concept of backscattering

When an interrogation signal is transmitted from the reader towards a target, the target scatters a part of the interrogation signal back to the reader. This scattered signal is called the backscatter and the process is called backscattering. Geometry, composition, distance of the target from the reader, the interrogation frequency and polarization decide the characteristics of backscattered signal [17].

As shown in Figure 3.1 when the interrogating antenna transmits an interrogation signal towards an antenna sensor, the backscattered signal consists of two components, the structure mode backscatter and the antenna mode backscatter [23][11].

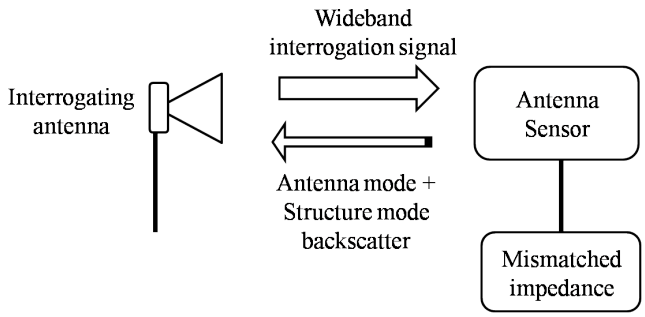

Figure 3.1. Antenna sensor backscattering modes.

3.2.1 Antenna mode backscatter

Being an antenna by itself, the antenna sensor excites its dominant modes at their corresponding resonant frequencies when a wideband interrogation signal is incident on it. Due to the dominant modes of the antenna sensor, it receives the interrogation signal at frequencies equal to its resonant frequencies, much like a frequency filter. If the antenna sensor is not terminated with a matched impedance, the received signal gets reflected at the mismatched termination and gets re-radiated from the antenna sensor. This re-radiated signal is called the antenna mode backscatter. The dominant frequencies of antenna mode backscatter are the same as the resonant frequencies of the antenna sensor.

3.2.2 Structure mode backscatter

The structure of the antenna sensor by itself reflects the interrogation signal back towards the reader. This backscattered signal is called the structure mode backscatter. Physical structural components of the antenna sensor also contribute to the structure mode backscatter. This type of backscattering is independent of the antenna sensor resonant frequency. The structural mode backscatter is typically one

to two orders of magnitude greater than the antenna mode backscatter and dominates the antenna mode backscatter.

3.3 Backscattering normalization

It follows from the discussion that when an antenna sensor is incident with wideband interrogation signal, the backscattered signal consists of two components, antenna mode backscatter and structure mode backscatter. The structure mode backscatter dominates the antenna mode backscatter having a frequency spectrum same as that of the antenna sensor resonant frequency band. In order to measure an antenna sensor without physically connecting to it, it is necessary to cancel the structural mode backscatter and isolate the antenna mode backscatter using a suitable backscatter normalization scheme.

3.3.1 Concept

When an antenna is incident with wideband interrogation signal, the structure mode backscatter is independent of the antenna termination load. Changes in antenna termination load will only change the antenna mode backscatter. When the antenna termination load changes from an open circuit to a short circuit or vice-versa, the phase of the antenna mode backscatter shifts by 180° [11][17]. Thus, subtracting two backscatter measurements, one acquired with an open terminated antenna sensor and another with a short terminated antenna sensor, will cancel out the structure mode while doubling the antenna mode backscatter. In time domain, typically, the antenna mode backscatter and the structure mode backscatter occur at almost the same instant of time. Alternatively, the antenna mode backscatter can be delayed in time with respect to the structure mode backscatter by using a delay line between the antenna sensor and its terminating impedance as shown by Hu et al. [17].

3.3.2 Backscatter normalization using microwave switch

In order to switch the antenna sensor impedance from open circuit to short circuit, a microwave relay switch can be used. The microwave relay switch can be used to connect the antenna sensor either to an open circuit termination or a short circuit termination by controlling the switching signal. In order to test this concept, an off-the-shelf microwave relay switch (Minicircuits model MSP2T-18) was used. An experiment setup as shown in Figure 3.2 was used to test the performance of the microwave relay switch. The microwave switch was connected to Port 1 of a VNA (Model ZVA-24, Rohde & Schwarz) configured to measure its S_{11} parameter from 1 GHz to 18 GHz. Two frequency domain measurements were acquired, one with the switching signal turned on and another with the switching signal turned off. These two measurements were processed with Inverse Fast Fourier Transform (IFFT) to generate time domain responses of the measurements. The phases of these two measurements were compared in time domain to determine the phase shift between open circuit termination and short circuit termination.

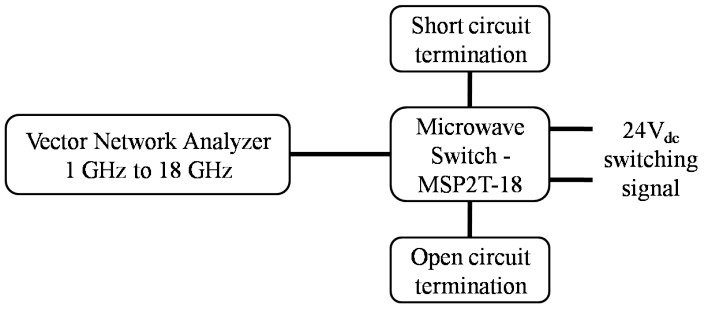

Figure 3.2. Impedance switch test setup.

Once the microwave switch operation was verified, it was connected to an antenna sensor with resonant frequencies of 6.9 GHz and 8.2 GHz. The antenna sensor was placed at a far field distance of 53 inches from an interrogating horn antenna

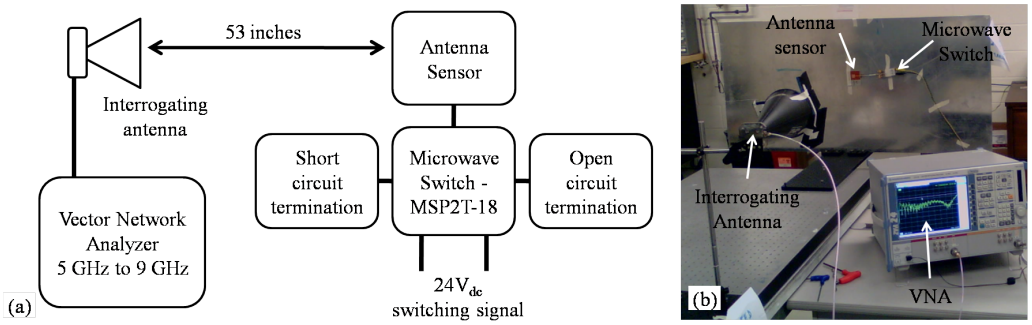

Figure 3.3. Normalization switch test:(a)schematic; (b)experiment setup.

(Singer Model A6100) as shown in Figure 3.3. The interrogating antenna was connected to port 1 of a VNA (Model ZVA-24, Rohde & Schwarz) configured to measure S_{11} parameter from 5 GHz to 9 GHz in 2000 points. Two measurements were taken corresponding to the two switching states of the microwave switch. The structure mode backscatter remains constant between the two measurements while the antenna mode backscatter shifts its phase by 180°. Thus, subtracting these two measurements cancels the structure mode backscatter to yield the normalized backscatter signal.

3.3.3 Implementation of impedance switch in antenna sensor

The electro-mechanical microwave switch (model MSP2T-18) previously used requires 24V at around 100mA to perform the switching. Due to this power requirement, it cannot be used in practical applications requiring the antenna sensor to be passive and completely wireless. In addition, the large physical footprint of the switch makes it impractical for application in antenna sensors. For this reason a pseudomorphic high electron mobility transistor (pHEMT), model ATF36077 from Avago Technologies, was selected to perform the impedance switching function. This device has good performance characteristics in the microwave frequency band and is a discrete device available in a microstrip package [12].

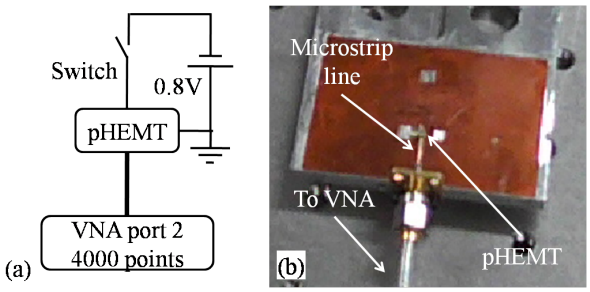

Figure 3.4. pHEMT switching test setup:(a)schematic; (b)experiment setup.

In order to verify the switching properties of the pHEMT over the desired frequency range, an experiment setup shown in Figure 3.4 was used. The pHEMT, mounted on a dielectric substrate, was connected to the VNA (Model ZVA-24, Rohde & Schwarz) through a SMA connector by connecting its drain terminal and the pin of the SMA connector using a microstrip transmission line. The source terminal of the pHEMT was connected to the ground. The VNA was set to measure the S_{11} parameter from 3 GHz to 10 GHz with 4000 points. Complex frequency domain response of port 1 was measured using the S_{11} parameter. This complex frequency domain response was then processed using inverse fast Fourier transform (IFFT) to obtain time domain response of the experiment setup. The time domain response corresponding to the pHEMT was then time gated and processed with fast Fourier transform (FFT) to obtain frequency domain response of the pHEMT. Phase information from this frequency domain response was extracted to get a plot of phase response of the pHEMT over frequency domain. This experiment was performed for gate terminal voltages of 0 V and -0.8 V, corresponding to the case when the pHEMT was in saturation mode and in cutoff mode, respectively. The resultant phase - frequency plots were subtracted to obtain a phase difference plot in frequency domain. This plot gives the actual phase response of the pHEMT between its cutoff and saturation modes.

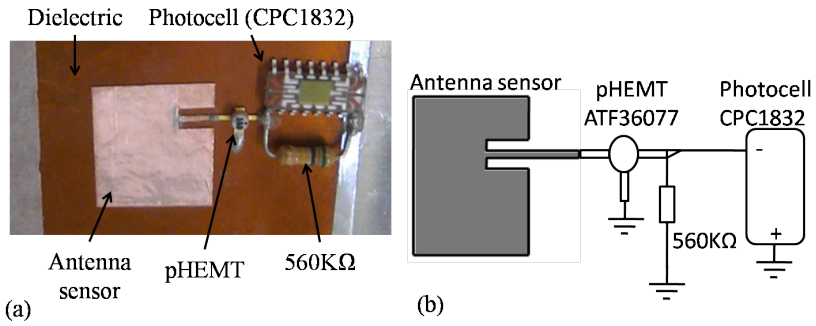

Figure 3.5. Antenna sensor implementation:(a)schematic; (b)implementation.

After the switching properties of the pHEMT was verified, a light-activated switching circuit was implemented using the pHEMT and a photocell (Clare model CPC 1832). The integration of the antenna sensor and the light-activated switching circuit is shown in Figure 3.5. The antenna sensor was fabricated by bonding a dielectric substrate (Kapton HN, 125 μm in thickness, dielectric constant $\epsilon_r = 2.5$) on an aluminum block using super glue, followed by bonding the patch antenna on the dielectric substrate, again using super glue. The antenna sensor pattern and the transmission line were cut from a copper tape (3M 1181, 26 μm in thickness, 12.75 mm in width and 15 mm in length) using a sharp blade. The source terminal of the pHEMT, the anode of the photocell and the ground of the 560 kΩ resistor were bonded to the antenna sensor ground plane using conductive epoxy. The inset-fed patch antenna was connected to the drain terminal of the pHEMT through a microstrip transmission line. The gate terminal of the pHEMT was connected to the cathode of the photocell.

The pHEMT offers an open circuit from its drain terminal to the ground plane when its gate voltage is kept at -0.8 V and a short circuit when its gate voltage is 0 V. The 580 kΩ resistor was employed to reduce the voltage output (at constant current) of the photocell from an open circuit value of 8 V to 0.8 V when it was exposed to

a light beam generated by a flashlight. The photocell was operated in saturation to make sure that it produced a stable output. It was observed that the ambient light was not sufficient to cause any change in the pHEMT biasing.

3.4 Summary

In this chapter, an impedance switching based normalization scheme has been developed to isolate the antenna mode backscatter while canceling the structure mode backscatter. The working of this normalization scheme has been verified using a microwave relay switch. In order to implement this normalization scheme on an antenna sensor, the microwave relay switch was replaced with a pHEMT device to make the normalization circuit compact and reduce the power requirement.

CHAPTER 4

WIRELESS ANTENNA SENSOR INTERROGATION

4.1 Introduction

This chapter describes the experiment setup and the signal processing algorithm required to interrogate an antenna sensor. A brief account on the power budget analysis has been presented to estimate the maximum interrogation distance from the reader to the antenna sensor. An experiment is described to determine the ability of the interrogation scheme to measure the antenna sensor at different angles of incidence.

4.2 Antenna sensor interrogation setup

The experiment setup used to interrogate an antenna sensor is shown in Figure 4.1. The antenna sensor was placed in the far-field region of an interrogating horn antenna connected to a VNA. A light source was placed pointing at the photocell in the antenna sensor. The light source and the VNA were controlled by a program developed using Microsoft Excel VBA. A wideband horn antenna, Singer instruments model A6100, was used as the interrogation horn antenna. The antenna sensor and the light-activated impedance switching circuit were implemented on an aluminum block, which was then mounted on a large aluminum sheet that imitated a large metallic structure. The distance between the antenna sensor and the horn antenna was 53 inches. The interrogating horn antenna was connected to port 1 of the VNA, which was programmed to measure the S_{11} parameter from 5 GHz to 9 GHz in 4000 points. The VNA was calibrated with its reference plane at the horn antenna

feeding point and the output power of the VNA was set at 20 dBm. A flashlight was used as the light source. To control the flashlight using the MS Excel control program, the flashlight was connected to a power supply through a relay switch (OEG model OUAZ-SS-105D). A parallel port of a computer, which will be referred to as the control computer from here on, was used to generate the switching signal for the relay. The VNA was connected to the control computer using an Ethernet cable. An Excel sheet VBA based control program was developed to initiate the VNA at the beginning of the test, trigger the VNA to collect S_{11} data at different antenna termination states, receive data from the VNA and store the data in the hard disk of the control computer. The same program also controlled the light source so that the impedance switching of the antenna sensor termination and the data collection were synchronized. The measurement was done in two steps. The spectrum of the backscatter signal was first measured when the light source was turned off. At this state, the pHEMT was in saturation mode and the antenna sensor was short circuit terminated. The light source was then turned on to bias the pHEMT into the cut-off mode and thus terminate the antenna sensor with open circuit impedance. The VNA was again triggered to collect the spectrum of the backscatter signal. The measured spectra were downloaded from the VNA to the control computer for data processing.

4.3 Dual frequency antenna sensor interrogation

A rectangular patch antenna can radiate at two fundamental radiation modes: the TM_{01} mode which is polarized along the length dimension of the antenna sensor patch, while the TM_{10} mode which is polarized along the width dimension of the antenna sensor patch [34]. As long as the antenna sensor patch is not square, the antenna sensor will display two resonant frequencies, each corresponding to a dominant mode. These two resonant frequencies, denoted as f_{01} and f_{10}, can be interrogated

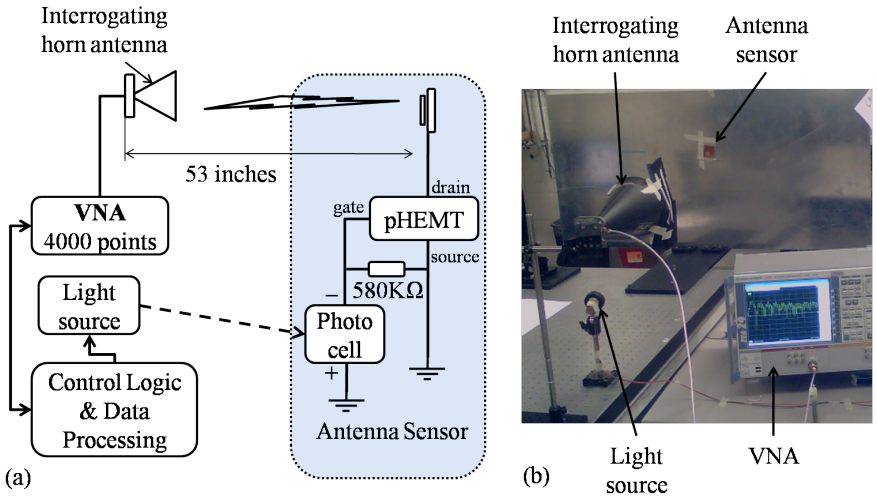

Figure 4.1. Antenna sensor interrogation:(a)schematic; (b)experiment setup.

separately by aligning the polarization of the interrogating signal parallel to the polarization direction of a particular dominant mode. For example, the interrogating horn antenna used in Figure 4.1 has two feed connectors: one for vertical polarization and the other for horizontal polarization. As shown in Figure 4.2(a), in order to interrogate the antenna sensor frequency associated with the width dimension of the antenna sensor patch, namely the f_{10} frequency, the connector of the interrogating horn antenna for vertical polarization was connected to the VNA. In Figure 4.2(b), the VNA connection was switched to the horizontal polarization to interrogate the f_{01} frequency.

4.4 Signal processing algorithm

Two sets of backscatter signals presented in frequency domain were acquired using the VNA at the two termination states of the antenna sensor. These two sets of data should be subtracted to isolate the antenna mode backscatter from the structural mode backscatter. In addition, VNA measures the frequency components of

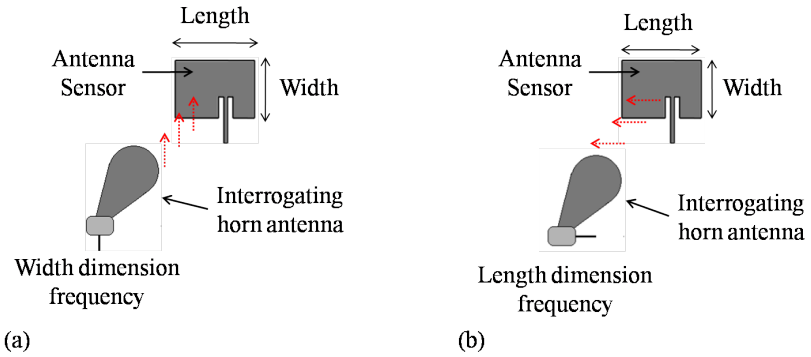

Figure 4.2. Interrogation of dual frequency antenna sensor.

backscatter signal over a long time span. The occurrence of antenna mode backscatter, on the other hand, is determined by the distance between the interrogating antenna and the antenna sensor. Therefore, the signal-to-noise ratio (SNR) of antenna mode signal can be improved by time gating the normalized backscatter signal. In order to perform time gating, the frequency domain signal measured by the VNA must be converted into time domain first. After time gating, the time domain antenna mode signal again needs to be converted back to frequency domain to extract the resonant frequency of the antenna sensor. Thus, a digital signal processing program is needed to implement the time gating, the frequency - time domain inter-conversions and the normalization scheme.

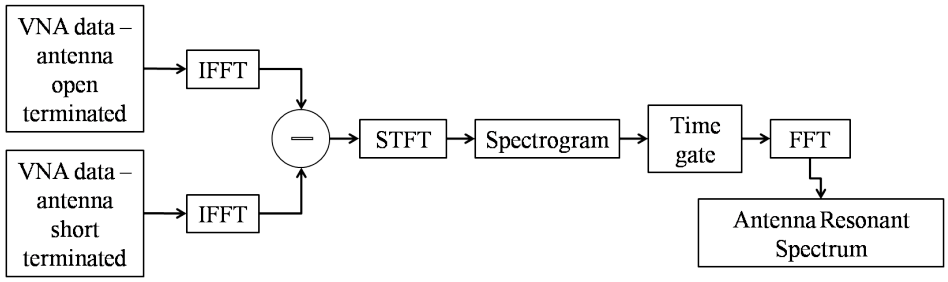

Figure 4.3. Signal processing algorithm.

A flow diagram of the signal processing algorithm is shown in Figure 4.3. The two measurement data files were imported into the program first. Subsequently, the frequency domain signals were converted to time domain signals using inverse fast Fourier transformation (IFFT). The time domain signals were then subtracted to obtain a normalized backscatter signal composed mainly of the antenna mode backscatter. Next, a short-time Fourier transformation (STFT) was performed to display the timefrequency components of the normalized signal, based on which the starting and ending time of the antenna mode backscatter can be selected. Finally, the normalized antenna mode backscatter signal was suitably time gated and converted to frequency domain using fast Fourier transformation (FFT). Based on the frequency spectrum of the time-gated antenna mode backscatter, the resonant frequency of the antenna sensor corresponding to the polarization of the interrogating signal can be determined.

4.5 Power budget analysis

The power received by the antenna sensor P_{rs}, placed at a distance R from the interrogating horn antenna, can be calculated from the Friis transmission equation [3] as

$$P_{rs} = P_t(\frac{\lambda}{4\pi R})^2 G_h G_s, \tag{4.1}$$

where G_h and G_s are the gains of interrogating horn antenna and the antenna sensor, respectively. λ is the wavelength of the interrogation signal and P_t is the power of the interrogation signal. When the pHEMT is in saturation mode, the pHEMT introduces an insertion loss due to the impedance mismatch between the microwave switching

circuit and the patch antenna. Therefore, the power of the signal that passes through the pHEMT and reaches the ground is given by

$$P_{ts} = D_{ds} \times P_{rs}, \tag{4.2}$$

where D_{ds} is the insertion loss of the pHEMT for signals transmitting from the drain terminal to the source terminal. Reflected by the ground, the signal has to go through the pHEMT again to reach the patch antenna. As a result, the power of the signal that is reflected back to the patch antenna is

$$P_{bs} = D_{sd} \times P_{ts} = D_{ds} \times D_{sd} \times P_{rs}, \tag{4.3}$$

where D_{sd} is the insertion loss experienced by the signal transmitted from the source terminal to the drain terminal of the pHEMT. The reflected power P_{bs} is transmitted by the patch antenna and received by the interrogating horn antenna. The received power at the interrogating horn antenna is again calculated from the Friis transmission equation, i.e.

$$P_{r,st} = P_{bs}(\frac{\lambda}{4\pi R})^2 G_h G_s. \tag{4.4}$$

Substituting equation 4.1 and equation 4.3 into equation 4.4, we have

$$P_{r,st} = P_t(\frac{\lambda}{4\pi R})^4 {G_h}^2 {G_s}^2 D_{ds} D_{sd}. \tag{4.5}$$

When the pHEMT is in cut-off mode, the patch antenna is open circuit terminated. Similarly, the power of the signal received by the horn antenna when the antenna sensor is open terminated is calculated as

$$P_{r,op} = P_t(\frac{\lambda}{4\pi R})^4 {G_h}^2 {G_s}^2 S_{11}, \tag{4.6}$$

where S_{11} is the S-parameter measuring the reflection from the pHEMT. The power of normalized antenna mode is then given by

$$P_r = P_{r,op} + P_{r,st} = P_t(\frac{\lambda}{4\pi R})^4 {G_h}^2 {G_s}^2 (S_{11} + D_{ds}D_{sd}). \tag{4.7}$$

In order to interrogate the antenna sensor with a required SNR, the power of the normalized antenna mode should satisfy

$$P_r \geq NF \times SNR, \tag{4.8}$$

where NF is the noise figure of the measurement system. The maximum distance R_{max} at which the sensor can be successfully interrogated, therefore, can be derived from equation 4.7 and equation 4.8 as

$$R_{max} = \frac{c}{4\pi f}\left[\frac{(S_{11} + D_{ds}D_{sd}) \times P_t \times {G_h}^2 {G_s}^2}{NF \times SNR}\right]^{1/4}. \tag{4.9}$$

4.6 Wireless interrogation angular response

In order to determine the advantages and potential limitations of the wireless interrogation scheme in different applications an angular response experiment was conducted on the antenna sensor wireless interrogation setup.

The antenna sensor was mounted on a rotation stage that allows it to be precisely rotated about three directions, i.e. the elevation, azimuth, and polarization direction. The antenna sensor was placed at a distance of 53 inches from the interrogating horn antenna. The antenna sensor was oriented in such a way that the polarization axis was parallel to the axis of the interrogating horn antenna, the el-

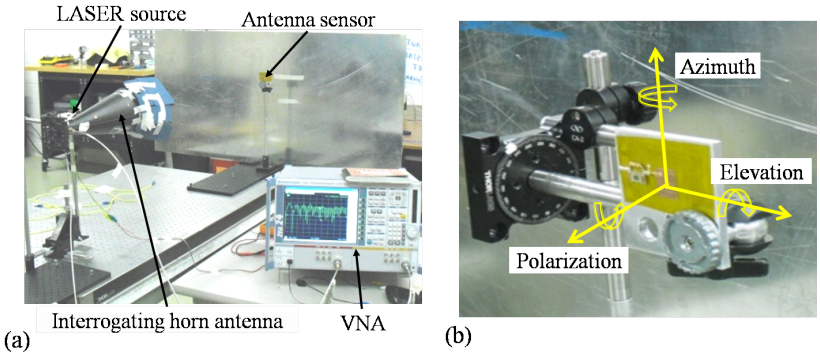

Figure 4.4. Angular response measurement setup.

evation axis was parallel to the antenna sensor length direction, and the azimuth axis was parallel to the antenna sensor width direction. A laser pointer, acting as the impedance switching light source, was placed next to the interrogating horn antenna, pointing at the photocell on the antenna sensor. The horizontal feed of the interrogating horn antenna was connected to the VNA.

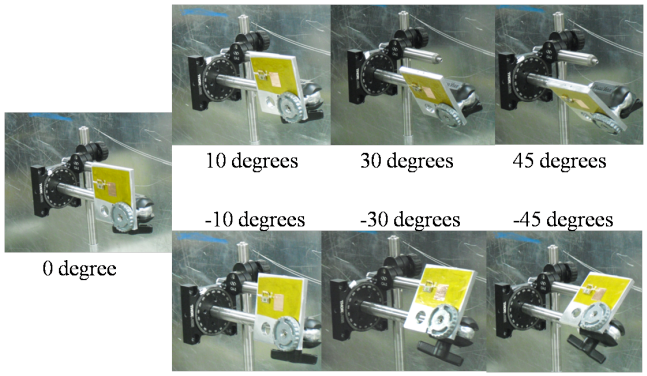

Figure 4.5. Elevation angle sweep of antenna sensor.

As such, the polarization of the interrogating horn antenna radiation was along the elevation axis, i.e. the length direction of the antenna patch. The VNA and the laser pointer were controlled by a computer to automate the process of measurements. The antenna sensor was interrogated at elevation angles of -45, -30, -10, 0, and 10

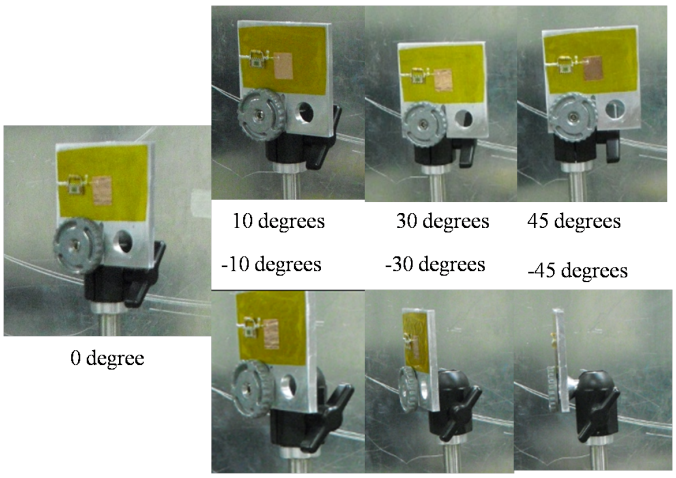

Figure 4.6. Azimuth angle sweep of antenna sensor.

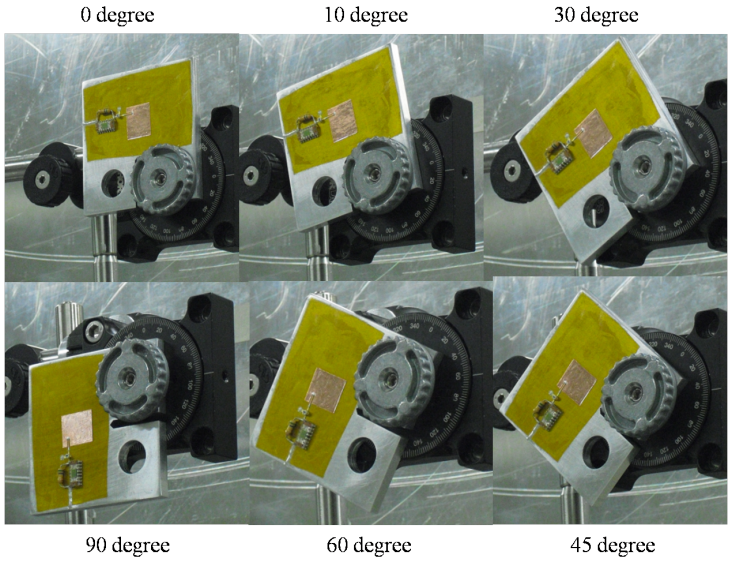

Figure 4.7. Polarization angle sweep of antenna sensor.

degrees as shown in Figure 4.5, azimuth angles of -45, -30, 0, 10, 30, and 45 degrees as showing in Figure 4.6, and polarization angles of 0, 10, 30, 45, 60, and 90 degrees as shown in Figure 4.7. The antenna sensor frequency spectrum measured for different elevation and azimuth angles were observed to determine the maximum elevation and

azimuth angles at which the antenna sensor can be interrogated with a good signal to noise ratio.

4.7 Summary

This chapter described the experiment setup and the signal processing algorithm required to wirelessly interrogate an antenna sensor. It also gave a brief account on the power budget model of the antenna sensor interrogation setup and the angular response of interrogation.

CHAPTER 5

RING RESONATOR BASED SENSORS

5.1 Introduction

This chapter presents the working of microstrip ring resonator and a preliminary study on its application for strain and crack sensing. Numerical simulations are presented to characterize the strain and crack sensing capabilities of different types of ring resonators.

5.2 Microstrip ring resonator

A microstrip ring resonator is a microstrip transmission line based resonator, conventionally consisting of a closed ring of transmission line. When energy is coupled into the ring, a standing wave is generated across the ring with maximum voltage at the point of coupling. A typical circular shape microstrip ring resonator is shown in Figure 5.1.

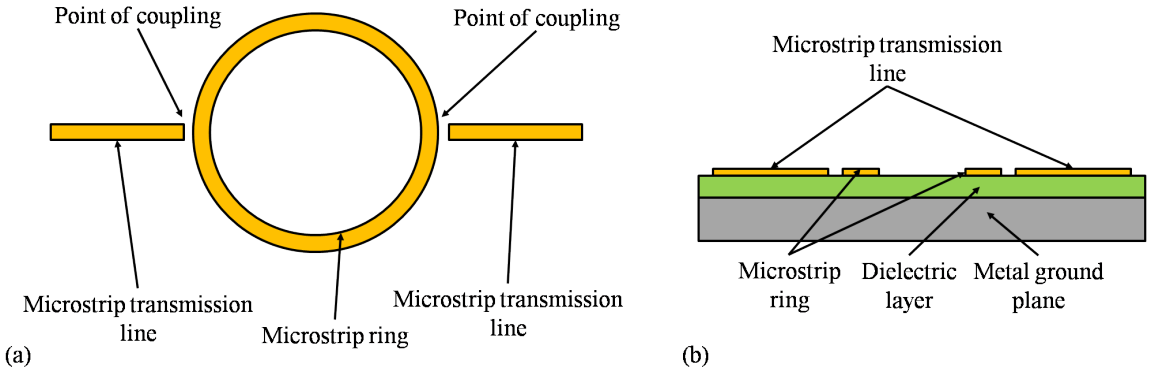

Figure 5.1. Circular microstrip ring resonator:(a)top view; (b)cross section.

In Figure 5.1, energy is coupled into the circular microstrip ring across the gap in between the ring and the microstrip transmission lines. The dimension of this gap decides the magnitude of coupling between the microstrip transmission line and the ring. Smaller gap will result in better coupling with lower insertion loss across the ring and low values of Q factor. Smaller gaps are typically used in microstrip filters. Larger gap will result in a loose coupling but a high Q factor [39][9]. Applications using ring resonators for measuring dielectric properties or change in dielectric properties due to physical measurands typically maintain larger gap in order to obtain high values of Q factor [27]. The coupling gaps act as capacitances and can lower the resonant frequency of the ring. Thus these coupling capacitances must be maintained to a minimum to avoid hampering the ring resonant frequency. The curvature of the ring affects the dispersion in the ring and the ring resonant frequency and hence needs to be carefully designed [38][22]. There are different types of coupling that can be used in microstrip ring resonators like loose coupling, matched loose coupling, enhanced coupling, annular coupling, direct coupling and side coupling [9][20]. A detail characterization of microstrip line based ring resonators has been dealt with by Bray et al. [4].

The condition for resonance in a microstrip ring is that the circumference of the ring must be equal to an integral multiple of the guide wavelength [27]. That is,

$$\lambda_g = \frac{S}{n} \quad where \;\; n = 1, 2, 3, 4, ... \tag{5.1}$$

where, S is the circumference of the ring and λ_g is the guide wavelength which is a function of the effective dielectric constant and frequency. From Equation 5.1, the fundamental resonant frequency of the ring is given by

$$f = \frac{c}{S\sqrt{\epsilon_r}}, \tag{5.2}$$

where c is a constant equal to the velocity of light in vacuum, ϵ_r is the relative permittivity of the dielectric layer below the ring and S is the circumference of the ring.

Numerous variants of the ring resonator suited for different applications have been developed. Ring resonator model proposed by Wu et al. [39] offers low insertion loss values while improving on the out-of-band suppression offered by generic coupled line filters.

5.3 Ring resonator as a strain sensor

The ring resonator resonant frequency is sensitive to changes in its circumference and relative dielectric constant as shown in Equation 5.2. An increase in the circumference of the ring will cause the resonant frequency to decrease. Thus, for a given dielectric constant, the circumference of the ring can be correlated to the ring resonant frequency. This concept can be applied to employ the ring resonator as a strain sensor. When a ring resonator is bonded on a structure, the ring resonator changes its dimensions depending on the strain experienced. Change in dimensions translate to a change in its circumference, thus changing its resonant frequency. In this section, two different shapes of ring resonators are studied to estimate the sensitivity of their resonant frequency to strain.

5.3.1 Square ring resonator

Consider a square ring resonator with a length 'b' and width 'a', where a is less than b, as shown in Figure 5.2. Now, if the strain is applied along the length dimension as shown in Figure 5.2, the circumference of the ring is given by

$$S = 2(1 - \mu\epsilon)a + 2(1 + \epsilon)b, \tag{5.3}$$

where μ is the Poisson's ratio and ϵ is the strain.

From Equation 5.3, for a given Poisson's ratio, increase in strain increases the circumference of the ring and from Equation 5.2, decreases the resonant frequency. Since the width dimension is smaller than the length dimension, strain acting along the width dimension will not cause significant change in the ring circumference and hence can be ignored.

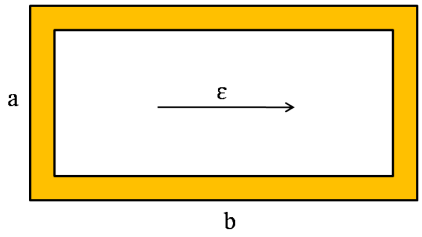

Figure 5.2. Square ring resonator.

In order to determine the effect of width and the effect of length on the sensitivity of ring resonator to strain, two sets of iterative numerical calculations were performed.

- First, at a constant arbitrary value of length, the strain sensitivity of the ring resonator was calculated for different values of width dimension by substituting Equation 5.3 into Equation 5.2. It was found that smaller width dimension resulted in higher sensitivity of ring resonant frequency to strain along the length dimension.
- The smallest possible ring width was calculated for a 50Ω impedance ring on a dielectric with ϵ_r equal to 2.5. With the ring width kept to this minimum

possible value, the sensitivity of ring resonator to strain was calculated for different values of length dimension.

5.3.2 Elliptical ring resonator

An elliptical ring resonator is shown in Figure 5.3. If the strain is applied along the major axis as shown in Figure 5.3, the circumference of the ring is given by [33]

$$S = \pi[(1-\mu\epsilon)a + (1+\epsilon)b]\left[1 + \frac{3(\frac{(1-\mu\epsilon)a-(1+\epsilon)b}{(1-\mu\epsilon)a+(1+\epsilon)b})^2}{10+\sqrt{4-3(\frac{(1-\mu\epsilon)a-(1+\epsilon)b}{(1-\mu\epsilon)a+(1+\epsilon)b})^2}}\right], \tag{5.4}$$

where μ is the Poisson's ratio, ϵ is the strain, a and b are the minor and major axis dimensions of the elliptical ring.

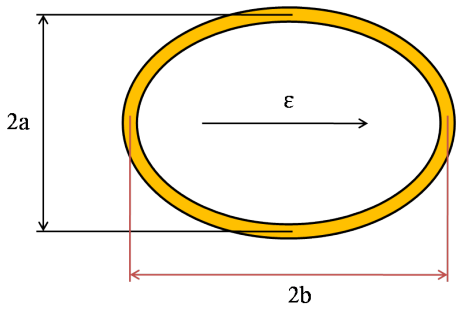

Figure 5.3. Elliptical ring resonator.

Based on Equation 5.4, for a given Poisson's ratio, an increase in strain increases the circumference of the ring and thus decreases the resonant frequency.

In order to determine the effect of minor axis and the major axis on the sensitivity of ring resonator to strain, two sets of iterative numerical calculations were performed.

- First, at a constant arbitrary value of the major axis dimension, the sensitivity of ring resonator to strain was calculated for different values of minor axis dimensions. It was found that smaller minor axis dimension resulted in higher sensitivity of ring resonant frequency to strain along the major axis.
- The smallest possible minor axis was calculated for a 50Ω impedance ring on a dielectric with ϵ_r equal to 2.5. With the minor axis dimension kept to this minimum possible value, the sensitivity of ring resonator to strain was calculated for different values of major axis dimension.

5.4 Ring resonator as a crack sensor

Conventional ring resonators have one fundamental frequency which is dependent only on the ring dimensions and the effective dielectric constant of the substrate below the ring. It has been shown that if the symmetry of the ring in the ring resonator is disturbed, two degenerate modes can be excited in the ring resonator [37]. The symmetry can be disturbed either by moving the feed points of the ring resonator closer on one side of the ring or by using a small notch on the ring resonator. Wolf et al. [37] also presented an experiment to determine the correlation between the notch depth and degenerate mode resonant frequency. It has been shown that the resonant frequency of the degenerate mode decreases with an increase in notch depth. This concept can be utilized to employ ring resonators for detecting and measuring structural cracks, for example around countersink screw holes. When the ring resonator is bonded on a structure, a structural crack can act as the notch and excite degenerate modes in the ring resonator. By measuring the resonant frequency of the degenerate modes, it is possible to determine the crack length in the structure. Figure 5.4 shows an example of a circular ring resonator employed to detect crack growing radially outwards from the screw hole.

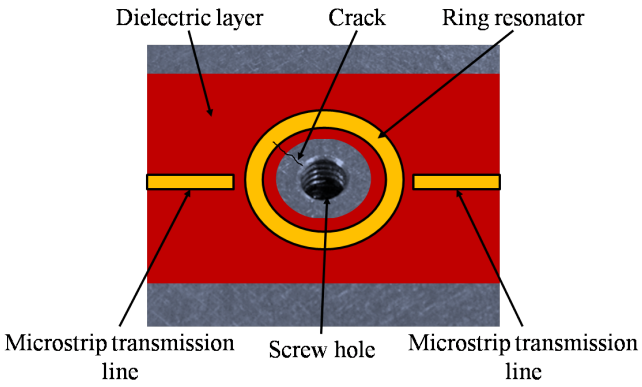

Figure 5.4. Example application of ring resonator based crack sensor.

In order to verify the concept of ring resonator as a crack sensor, ring resonator models were simulated on Sonnet EM simulation software. Circular and square shaped ring resonator models were simulated.

5.4.1 Circular ring resonator models

The generic circular ring resonator model is shown in Figure 5.5. The model is similar in layout to that described in Figure 5.1. The dielectric layer thickness was set to 50 μm and its dielectric constant, ϵ_r, was 2.5. The ground plane thickness or the structure thickness was 6 mm. Crack on the ring was simulated using a small crack 0.1 mm in width. Two microstrip transmission lines of width 0.5 mm were used to couple the ring resonator to ports 1 and 2. The ring width was maintained at 0.5 mm. The crack length was swept from 0 mm to 0.4 mm in steps of 0.1 mm. The simulator was configured to record the current plot of the ring resonator while simulating the S_{21} parameter.

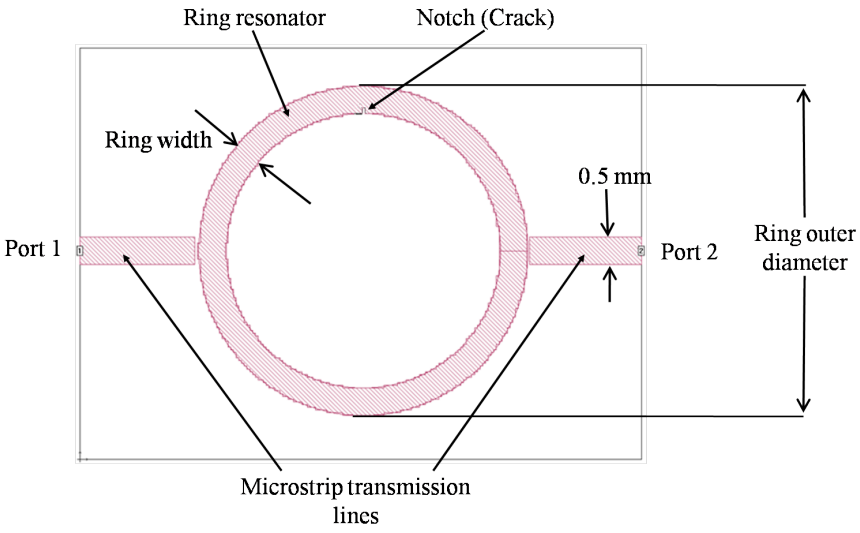

Figure 5.5. Generic circular ring resonator model.

5.4.1.1 Effect of ring size

In order to determine if the ring size had any effect on the sensitivity to crack, two simulations were run, one with a ring outer diameter of 9 mm and another with a ring outer diameter of 6 mm. The crack sensitivity plots were compared.

5.4.1.2 Effect of multiple rings with aperture coupling

The main purpose of this model was to determine if multiple concentric ring could be coupled in parallel to increase the crack detection area of the sensor. This model had two concentric rings fed from the microstrip transmission lines using aperture coupling. Figure 5.6 shows the simulation setup for this model. The simulator was setup to measure the S_{21} parameter of the model without the crack.

5.4.2 Rectangular ring resonator models

The generic rectangular ring resonator model is shown in Figure 5.7. The dielectric layer thickness was set to 50 μm and its dielectric constant, ϵ_r, was 2.5.

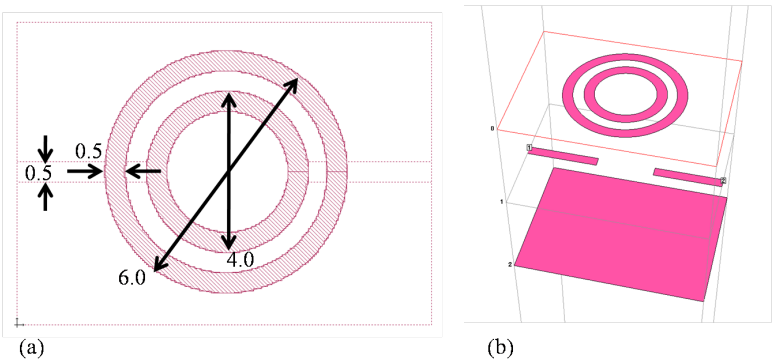

Figure 5.6. Aperture coupled concentric circular ring model.

The ground plane thickness or the structure thickness was 6 mm. Crack on the ring was simulated using a notch of 0.1 mm width. Two microstrip transmission lines of width 0.5 mm were used to couple the ring resonator to ports 1 and 2. The ring width was maintained at 0.5 mm. The crack length was swept from 0 mm to 0.4 mm in steps of 0.1 mm. The simulator was configured to record the current plot of the ring resonator while simulating the S_{21} parameter. The ring length was 5.0 mm and width was 2.7 mm.

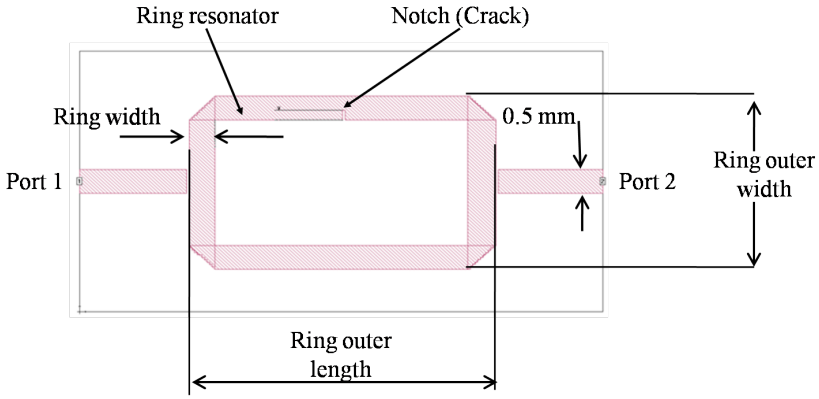

Figure 5.7. Generic square ring resonator model.

5.4.2.1 Effect of current density on crack sensitivity

The main purpose of this model was to determine the relation between sensitivity of the resonant frequency to crack and the current density on the ring at which crack propagates. The crack in the first model was at the center of the length dimension where the current density is maximum and in the second model, the crack was placed 0.5 mm from the ring edge, where the current density is considerably lower.

5.5 Summary

In this chapter, we have discussed the working of microstrip ring resonator and its application in strain and crack sensing. Numerical simulations were performed to study the working of different types of ring resonators for these applications. The numerical simulations gave a good account of what to expect when measuring practical models of ring resonators in strain and crack sensing applications.

CHAPTER 6

RESULTS AND ANALYSIS

6.1 Introduction

In this chapter, experimental results of the implementation of backscatter normalization scheme are discussed. The experimental results of power budget modeling and angular response of interrogation have been analyzed. Also, simulation results characterizing ring resonator as strain and crack sensor have been discussed. Sonnet EM Professional version 12.52 was used for EM simulation.

6.2 Impedance switch test

In this test, the backscatter normalization scheme concept was tested using an off-the-shelf microwave switch. Figure 6.1 shows the time domain response of the microwave switch for open circuit and short circuit termination cases. The 180° phase shift between the two cases is clearly visible.

Figure 6.2 shows the phase difference plot in frequency domain. It can be observed that the microwave switch is giving a fairly constant 180° phase shift between open circuit and short circuit termination cases from 1 GHz to 18 GHz. This is in good agreement with the expected response from the switch. This result can be taken as the ideal case for benchmarking other impedance switching mechanisms.

6.3 Microwave switch backscatter normalization test

Figure 6.3(a) and Figure 6.3(b) show the time domain backscatter when the antenna sensor is open circuit terminated and when it is short circuit terminated

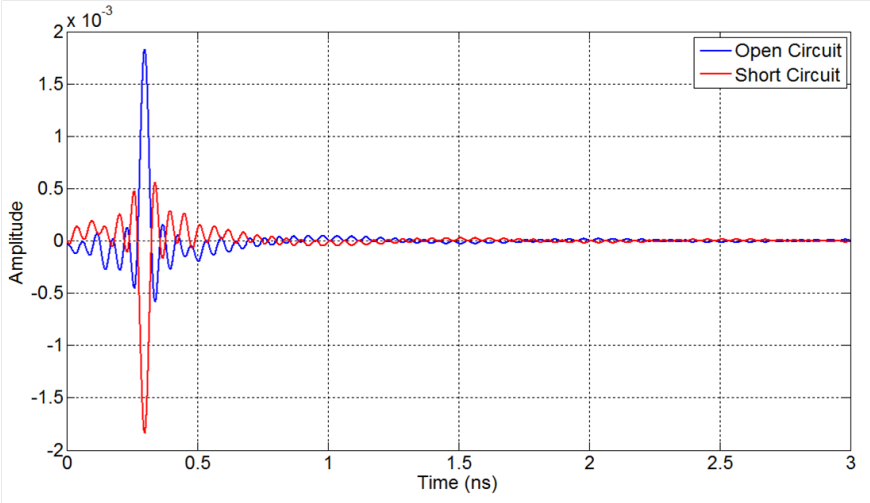

Figure 6.1. Impedance switch test: time domain response.

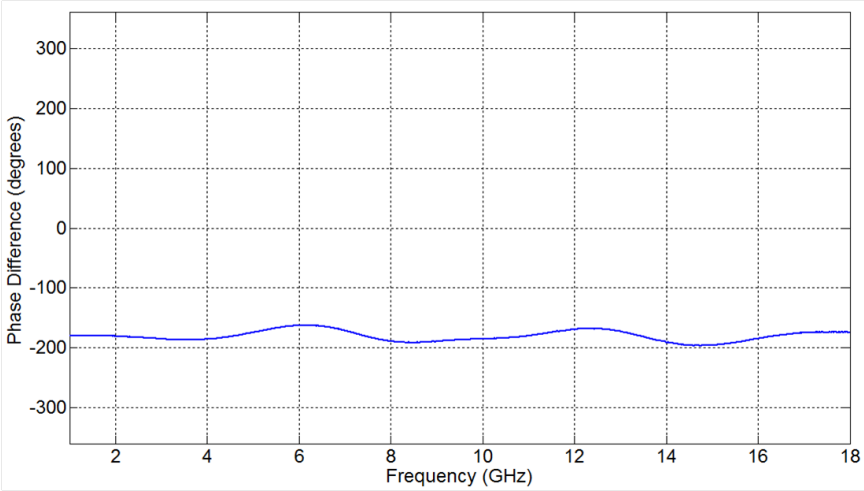

Figure 6.2. Impedance switch test: frequency domain phase response.

respectively. The two time domain plots look similar due to the common structure mode backscatter between the two.

Figure 6.4(a) shows the normalized backscatter signal in time domain. The antenna mode backscatter can be clearly observed starting at around 10 ns and ending at around 15 ns. Figure 6.4(b) shows the spectrogram of the normalized backscatter signal. The high intensity spot at around 10 ns time and 8.2 GHz frequency is the an-

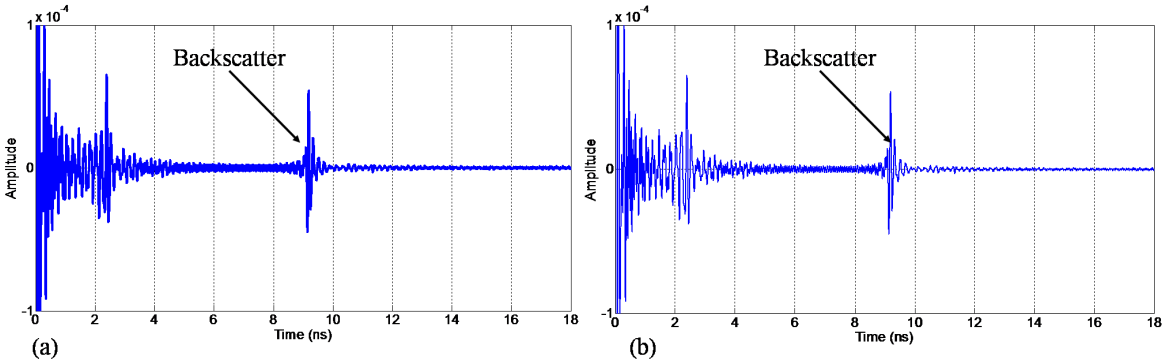

Figure 6.3. Time domain backscatter:(a)open circuit; (b)short circuit.

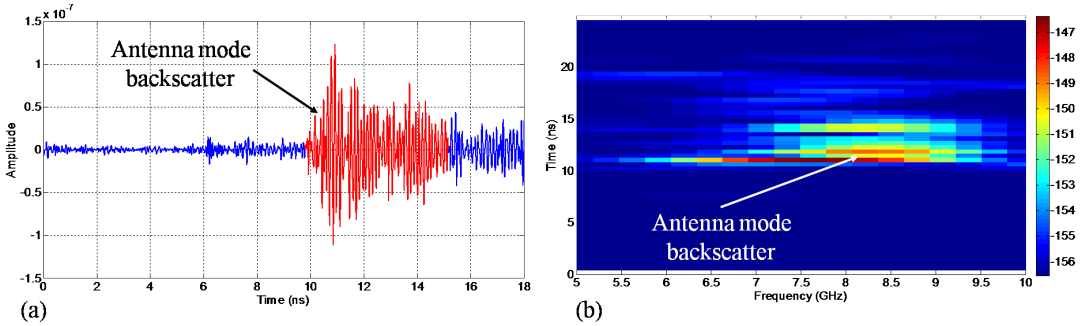

Figure 6.4. Normalized backscatter signal:(a)time domain; (b)spectrogram.

tenna mode backscatter. The resonant frequency of the antenna sensor, the dominant frequency component in the antenna mode backscatter can be clearly distinguished in this spectrogram. After time gating this antenna mode backscatter and processing it with fast Fourier transformation (FFT) algorithm we get the frequency domain plot of the antenna mode backscatter as shown in Figure 6.5.

The antenna sensor resonant frequency can be identified from Figure 6.5 as the frequency at which the amplitude response of the frequency domain plot is maximum. From Figure 6.5 it can be observed that the antenna sensor resonant frequency matches with that got from the antenna S_{11} plot shown in Figure 6.6. Thus it is evi-

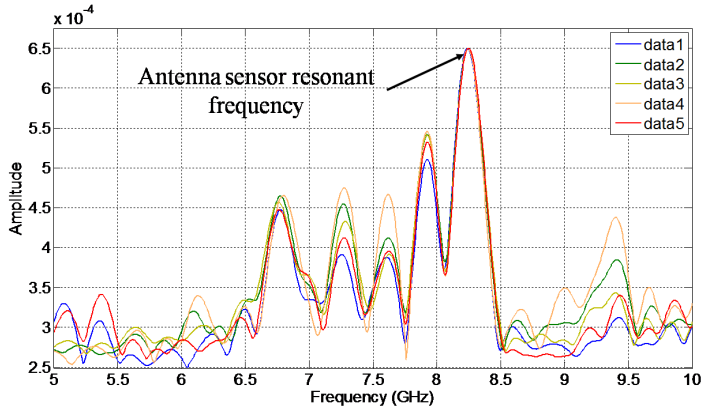

Figure 6.5. Frequency domain antenna mode backscatter.

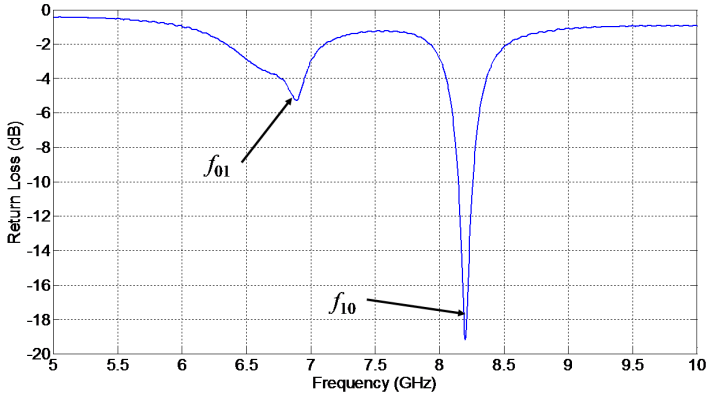

Figure 6.6. Antenna sensor S_{11} plot.

dent that the backscatter normalization scheme works successfully with off-the-shelf microwave switch.

6.4 pHEMT switching test

Figure 6.7 shows the amplitude response plot of the pHEMT device for cutoff and saturation modes over frequency range from 3 GHz to 9 GHz. The amplitude plots are relatively flat up to 7.5 GHz. The return loss of the pHEMT in saturation mode dips at around 4.1 GHz due to the loop resonance between the SMA connector and the ground plane. This resonance effect will not be present in the antenna sensor

since the SMA connector will be replaced by the patch antenna. The cutoff mode plot shows increased loss at frequencies greater than 7.5 GHz even though the pHEMT is rated to perform up to 18 GHz. The increased loss during cutoff mode is due to the experiment setup configuration causing stray resonances when the pHEMT is in high impedance state. In this case the losses could be corrected by redesigning the experiment setup with better matching between the SMA connector and the microstrip transmission line.

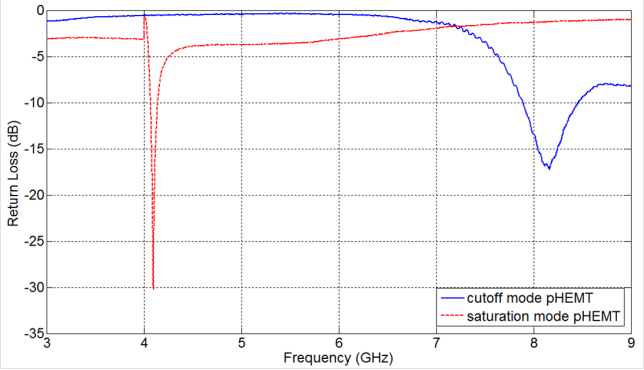

Figure 6.7. pHEMT amplitude response test.

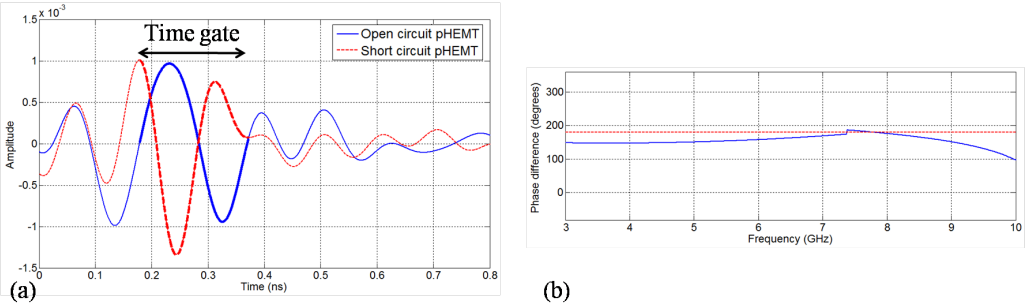

Figure 6.8. pHEMT phase response:(a)time domain; (b)frequency domain.

Figure 6.8(a) shows the phase response characteristics of the pHEMT test setup in time domain. After time gating the response of pHEMT device and processing it with fast Fourier transform (FFT), we get the frequency domain response of the pHEMT device. Figure 6.8(b) shows the frequency domain phase difference plot obtained after subtracting the phase responses of pHEMT device between cutoff and saturation modes. It can be observed from this plot that, on an average, the phase difference offered by the pHEMT from cutoff mode to saturation mode is 180°. This implies that the pHEMT device can be used for backscatter normalization scheme and its operation in this regard has been verified till 10 GHz.

6.5 Antenna sensor interrogation test

Figure 6.9(a) shows the time domain normalized backscatter signal. The antenna mode backscatter is clearly visible at around 9.5 ns. This agrees with the time taken for the EM wave to propagate the two-way distance between interrogating antenna and the antenna sensor. The high intensity signal at around 6.4 GHz is the antenna mode backscatter. After time gating the antenna mode signal and processing it with inverse fast Fourier transform (IFFT), we get the frequency spectrum of antenna mode signal. This experiment was repeated seven times for each of the two antenna sensor polarizations.

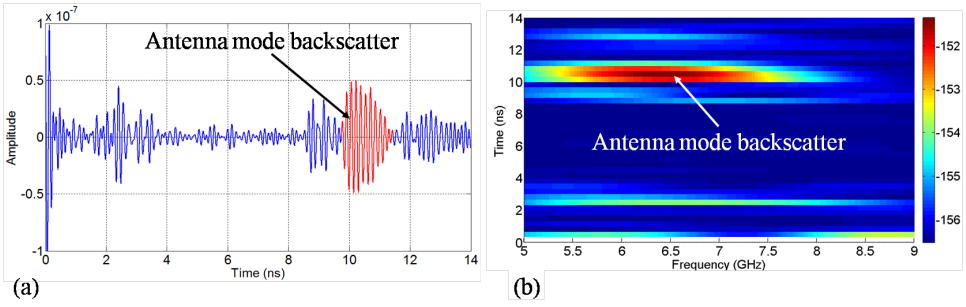

Figure 6.9. Normalized backscatter signal:(a)time domain; (b)spectrogram.

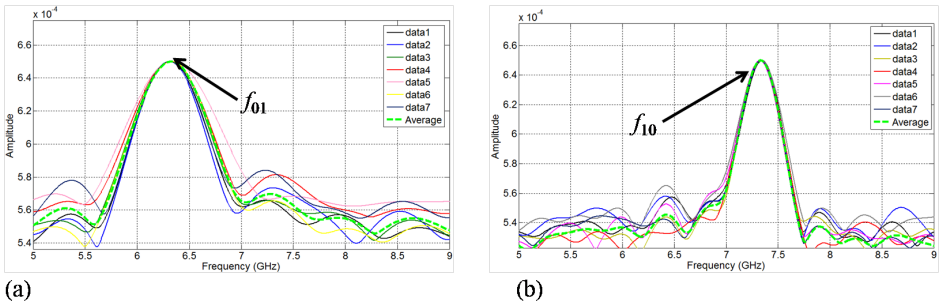

Figure 6.10. Antenna mode signal:(a)length dimension; (b)width dimension.

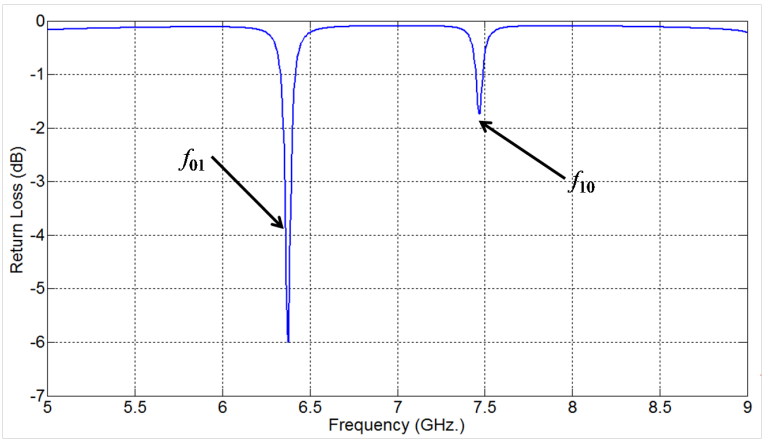

Figure 6.11. Simulated S_{11} plot of the antenna sensor patch antenna.

Figure 6.10(a) shows the frequency spectrum of the antenna mode backscatter for length dimension while Figure 6.10(b) shows the frequency spectrum of the antenna mode backscatter for width dimension. The resonant frequencies from Figure 6.10(a) and Figure 6.10(b) agree with the resonant frequencies obtained from the Sonnet EM simulation model of the antenna sensor. The simulated S_{11} plot of the antenna sensor is shown in Figure 6.11. SNR of the time-gated normalized antenna mode backscatter at f_{10} frequency was estimated to be approximately 1.16 (0.64 dB). Averaging the seven measurements improved the SNR only slightly. This indicates

that the noise floor is probably contributed by other deterministic scattering sources due to the imperfect normalization.

6.6 Power budget modeling

To measure the insertion losses of the pHEMT and the noise figure of the measurement system, the transmission S-parameters from the horn antenna to the patch antenna were first measured by connecting the horn antenna to port 1 of the VNA and the patch antenna to port 2 of the VNA. The S_{12} and S_{21} parameters were measured to be around -34 dB. Assuming the interrogation frequency is 7.5 GHz, the gain of the horn antenna is G_h = 12 dBi = 15.84, the gain of the antenna sensor is G_s = 6 dBi = 3.98 and the distance R = 53 inches = 1.34 m, the calculated horn antenna to patch antenna transmission loss is 34.5 dB, which matched with the measurements very well. Next, the switching circuit was added between the patch antenna and the port 2 of the VNA, as shown in Figure 6.12. When the pHEMT is in saturation, i.e. the patch antenna is short-connected to the SMA connector, the S_{12} and S_{21} parameters were measured to be 43.4 dB. Therefore, the insertion losses of the switching circuit, D_{ds} and D_{sd}, can be calculated from the S_{12} and S_{21} parameters measured before and after the switching circuit was inserted, i.e. D_{ds} = D_{sd} = 43.4 - 34.5 = 8.9 dB. The S_{11} parameter of the pHEMT in cutoff mode can be measured from Figure 6.7, which is around -1 dB. Substituting these parameters into Equation 4.7, the power of the normalized antenna mode signal is calculated to be -49.91 dBm, assuming the interrogation power is 20 dBm. The noise figure of the system can be then estimated from the calculated receiving power and the measured SNR to be -50.55 dBm, which is 12.55 dB higher than the noise figure of the VNA calculated from the specifications of the VNA. The additional noises are likely to be contributed by the surrounding medium and the structural mode backscattering

that was not completely canceled out by the normalization process. To increase the interrogation distance and the SNR, power of the interrogation signal and gain of the interrogation antenna should be increased. For example, increasing the power of the interrogation signal to 30 dBm and the gain of the interrogation antenna to 20 dB, the interrogation distance can be increased to 3.5 m with a SNR of 10 dB, assuming the other parameters remain the same ($D_{ds} = D_{sd} = 8.9$ dB and NF = -50.55 dBm). Reducing the insertion losses D_{ds} and D_{sd} of the switching circuit will also increase the interrogation range. However, their influences on the interrogation range are not very significant, based on Equation 4.9.

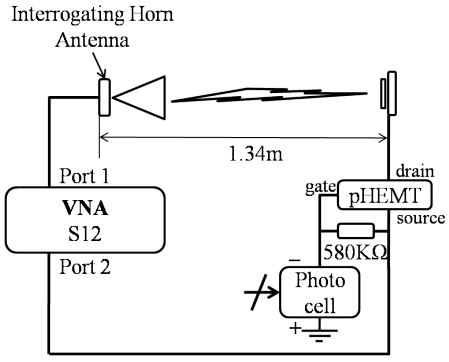

Figure 6.12. Insertion loss measurement setup.

6.7 Wireless interrogation angular response

The resonant frequency of patch antenna for various elevation, azimuth and polarization angles is shown in Figure 6.13, Figure 6.14 and Figure 6.15 respectively. For Figure 6.13 and Figure 6.14, the SNR was the highest when the antenna sensor was oriented at 0 degree. As the angle of rotation increased, the SNR reduced while the resonant frequency remained the same. This indicates that the antenna frequency measurement is not very sensitive to the angular alignment. The resonant frequency

of the antenna sensor can be reliably measured as long as the antenna sensor and the horn antenna are aligned within ±30 degrees along these two directions. Rotating the antenna sensor along the polarization direction essentially changes the orientation of the antenna patch relative to the polarization of the horn antenna radiation. At zero degrees, the length direction of the antenna patch was parallel to the polarization of the horn antenna radiation. As a result, only the f_{01} frequency was observed. As the rotation angle increased, the f_{01} frequency remained at the same position while the SNR decreased. At 60 degrees, the f_{10} frequency started to emerge and the f_{01} frequency disappeared. At 90 degrees, the width direction of the antenna patch was aligned with the polarization of the electromagnetic field. As such, only the f_{10} frequency was visible. This experiment demonstrated that the two fundamental resonant frequencies of the antenna sensor can be remotely interrogated using one rotating horn antenna or using a horn antenna with dual polarizations.

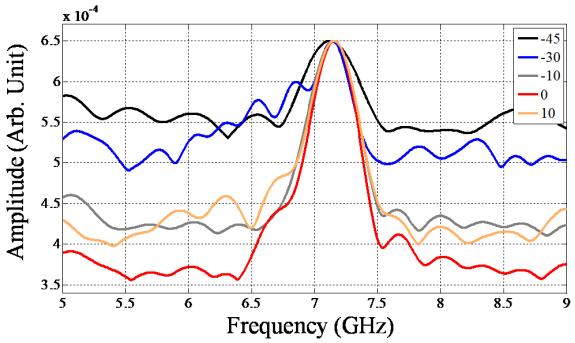

Figure 6.13. Elevation angle response of antenna sensor.

6.8 Ring resonator as a strain sensor

Figure 6.16 shows the change in strain sensitivity of resonant frequency with variation in width dimension of the ring resonator while the length dimension is

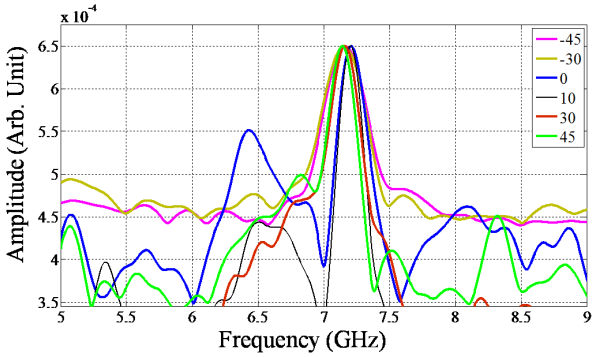

Figure 6.14. Azimuth angle response of antenna sensor.

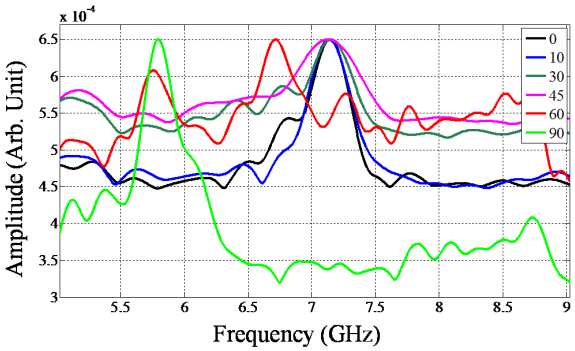

Figure 6.15. Polarization angle response of antenna sensor.

maintained a constant of 6 mm. In Figure 6.16, slope is the ratio of change in resonant frequency shift to change in percentage strain on the ring resonator. It can be observed that smaller width dimension resulted in higher strain sensitivity.

Keeping the width dimension at a minimum, Figure 6.17 shows the change in strain sensitivity with variation in the length dimension of the ring resonator. We can observe that larger length dimension results in higher strain sensitivity.

Figure 6.18 shows the change in strain sensitivity with variation in minor axis dimension of the elliptical ring resonator while the major axis dimension is maintained a constant of 6 mm. It can be observed that smaller minor axis dimension result in higher strain sensitivity.

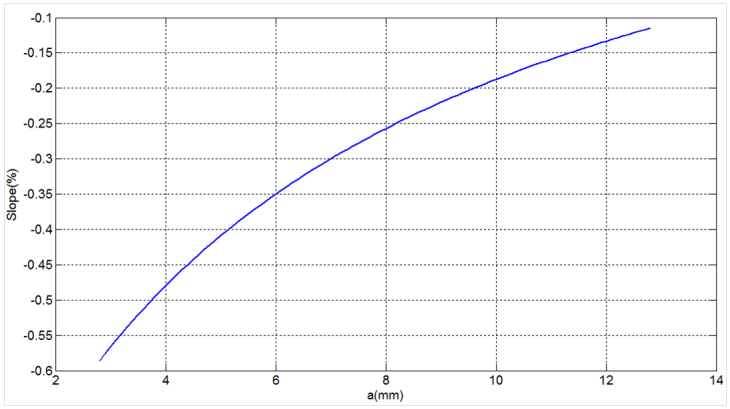

Figure 6.16. Variation of strain sensitivity with width dimension.

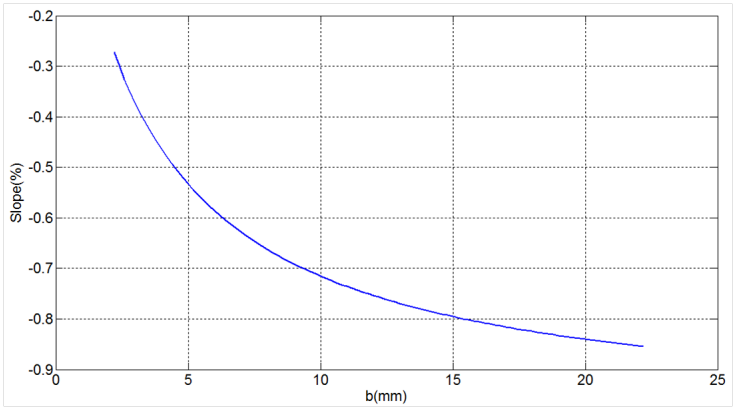

Figure 6.17. Variation of strain sensitivity with length dimension.

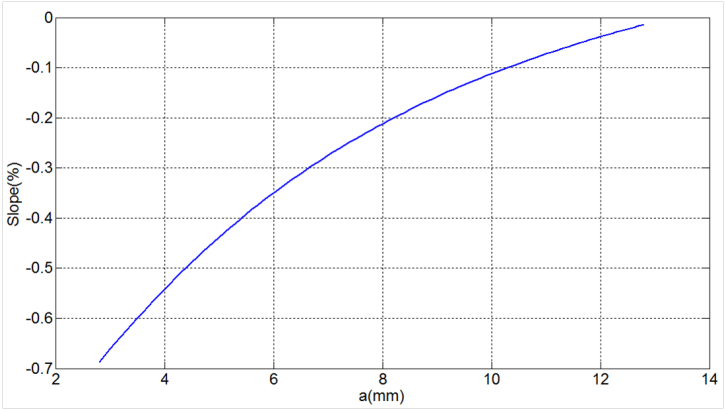

Figure 6.18. Variation of strain sensitivity with minor axis dimension.

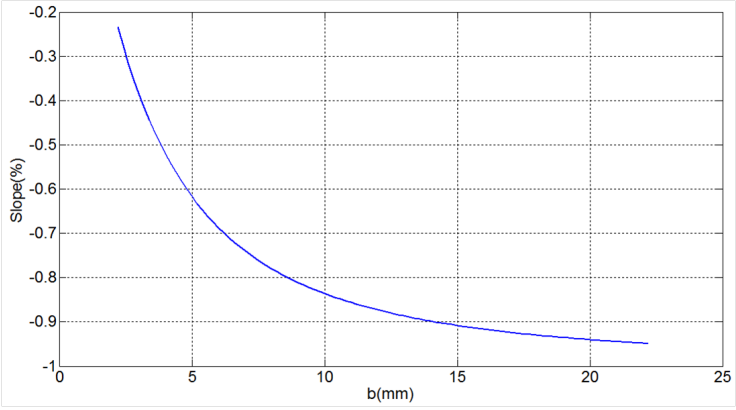

Figure 6.19. Variation of strain sensitivity with major axis dimension.

Keeping the minor axis dimension at a minimum, Figure 6.19 shows the change in strain sensitivity with variation in major axis dimension of the elliptical ring resonator. From this figure, we can observe that larger major axis dimension results in higher strain sensitivity.

6.9 Ring resonator as crack sensor

In order to characterize ring resonator based crack sensor models, a total of four simulations were performed using two shapes of ring resonators.

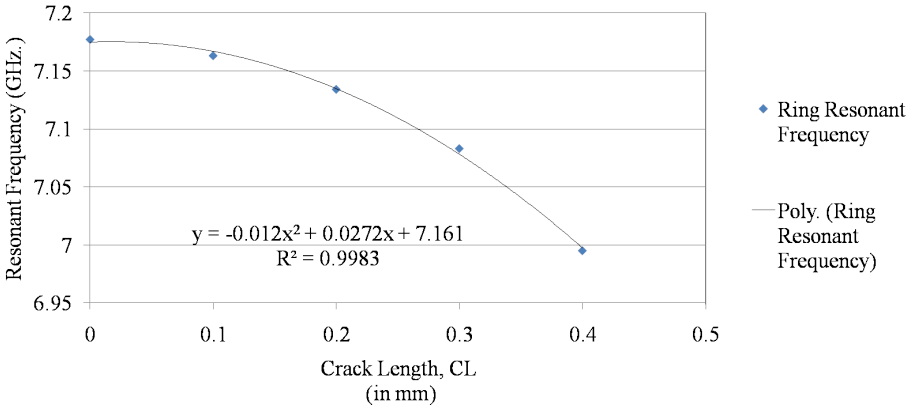

Figure 6.20. Crack sensitivity plot: 9 mm diameter ring.

In order to determine if the ring size had any effect on the sensitivity to crack, two simulations were run, one with a ring outer diameter of 9 mm and another with a ring outer diameter of 6 mm. Figure 6.20 shows a plot of crack length versus ring resonant frequency for a circular ring resonator with a ring outer diameter of 9 mm.

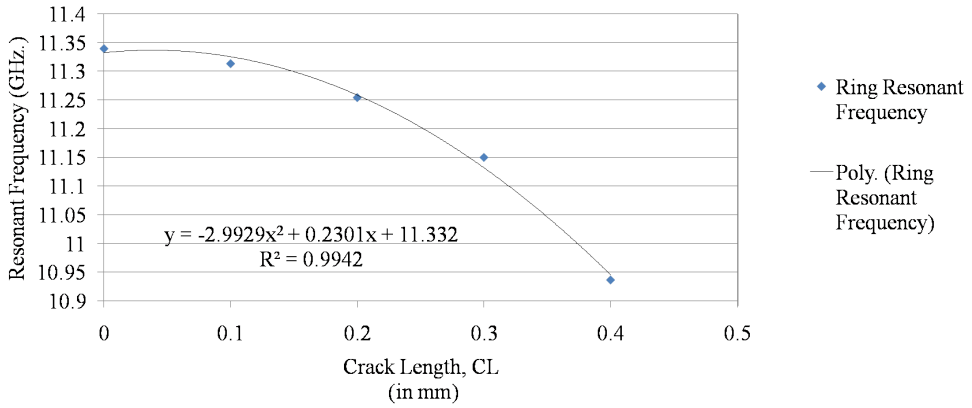

Figure 6.21. Crack sensitivity plot: 6 mm diameter ring.

Figure 6.21 shows a plot of crack length versus ring resonant frequency for a circular ring resonator with a ring outer diameter of 6 mm. Comparing Figure 6.20 and Figure 6.21 we infer that ring resonators with smaller diameters are more sensitive to crack than ring resonators with larger diameters.

A concentric dual ring resonator was simulated to determine if multiple concentric ring could be coupled in parallel to increase the crack detection area of the sensor. This model had two concentric rings fed from the microstrip transmission lines using aperture coupling.

Figure 6.22 shows the S_{21} plot of a ring resonator model with two concentric rings coupled using an aperture. The S_{21} plot shows two distinct peaks representing the resonant frequencies of the two concentric rings. Thus concentric ring resonators

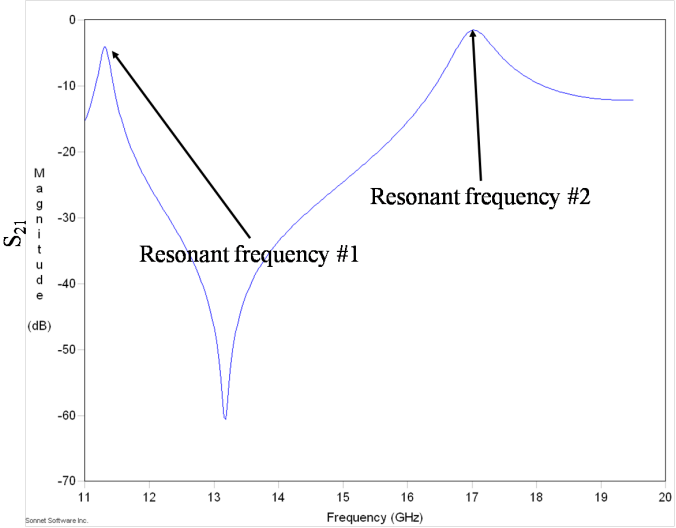

Figure 6.22. S_{21} plot: concentric circular rings.

may be used to increase the crack sensing area so long as the harmonic frequencies of one ring does not coincide with the fundamental frequency of another ring.

The current density on a ring resonator is not constant over its dimensions. The current density on a ring resonator is maximum at a distance of $\lambda_g/2$ from the coupling points and minimum near the coupling points. Two simulations were run to ascertain the effect of current density on the crack sensitivity of a ring resonator. One of the simulation models had the crack propagating in the high current density region while the other model had its crack propagating in the lower current density region.

Figure 6.23 shows the crack sensitivity plot of a ring resonator model having its crack in the high current density region. The corresponding current maps are shown in Figure 6.24.

Figure 6.25 shows the crack sensitivity plot of a ring resonator model having its crack in the low current density region. The corresponding current maps are shown in Figure 6.26. Comparing the crack sensitivity plots in Figure 6.23 and Figure 6.25,

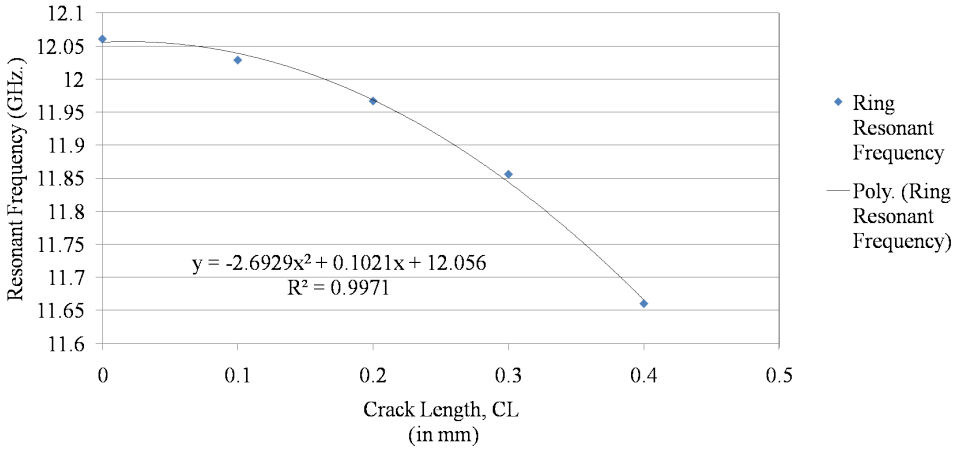

Figure 6.23. Crack sensitivity plot: crack in high current density region.

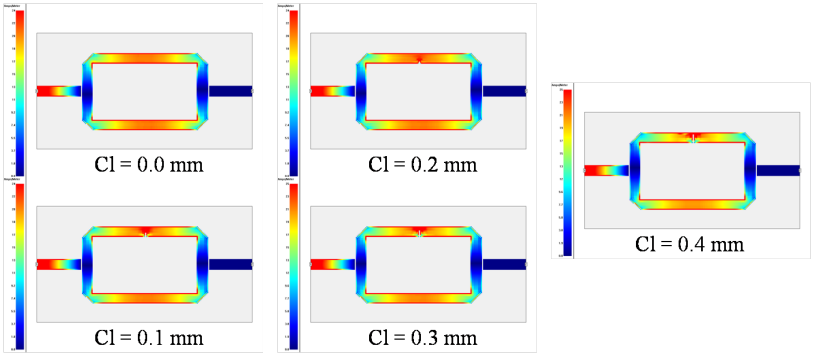

Figure 6.24. Current map: crack in high current density region.

it is evident that the crack sensitivity is higher when the crack propagation is in high current density regions of the ring resonator. This result has important implications on using the ring resonator for crack detection. It is important to have a prior knowledge of the crack sensitivity before installing a ring resonator based crack sensor. It is possible to have ambiguity about crack length and direction when the crack sensitivity of a ring resonator varies over its geometry. This issue can be solve by having two or more concentric ring resonators with coupling points alternatively offset by 90 degrees. The direction of crack growth can be determined by observing the change in resonant frequency of the two or more concentric rings.

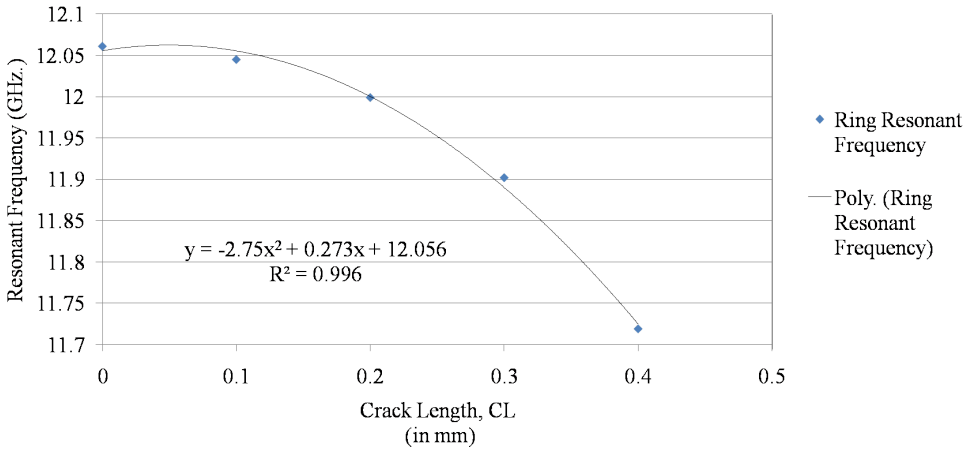

Figure 6.25. Crack sensitivity plot: crack in low current density region.

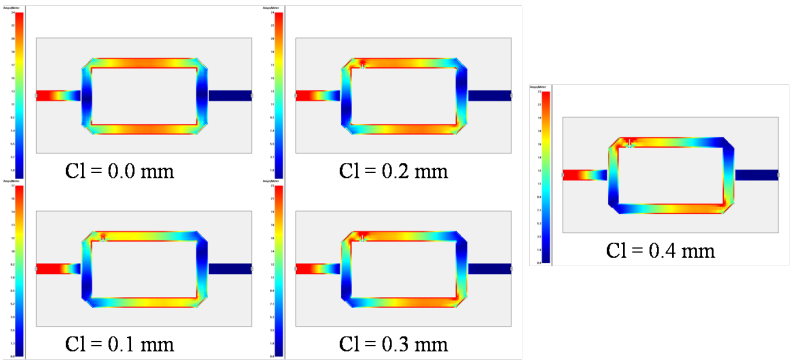

Figure 6.26. Current map: crack in low current density region.

CHAPTER 7

CONCLUSIONS

The wireless interrogation method presented in this paper enables the antenna sensor to be interrogated wirelessly without the aid of a power source on board the antenna sensor. Since there is no requirement for a power source on the antenna sensor, the antenna sensor is light weight, low cost and offers long operational life.

From the experimental results, a wireless antenna sensor operating at 6.3 GHz and 7.4 GHz can be interrogated from a distance of 1.34 meters with an antenna mode signal to noise ratio of 0.64 dB. The interrogation distance can be improved by using a high gain patch antenna for the antenna sensor and a high gain interrogating antenna. The interrogation distance can also be improved by increasing the interrogation power output. Angular response measurements show that an antenna sensor can be interrogated at upto ± 30 degrees from its normal and dual frequency antenna sensors can be interrogated by rotating the interrogating antenna polarization through 90 degrees.

Simulation results show that a ring resonator can be used to detect and measure structural cracks. The ring resonator based crack sensors are suited for detecting structural cracks near screw holes and other such closed-loop edges exposed to higher strain forces. The square ring resonator model simulations indicate that the square ring can detect cracks with consistently high sensitivity across its length dimension when coupling is placed at the width dimensions.

Future work will be focused on designing an RF activated normalization scheme instead of the light activated normalization scheme. An in-depth study to determine

the cause for the generation of degenerate modes in a ring resonator and their correlation to the asymmetry in the ring resonator will be performed. This will be accompanied by the fabrication and verification of the ring resonator crack sensitivity characteristics. The wireless interrogation scheme will also be incorporated to interrogate ring resonator based crack sensors.

APPENDIX A

DATA PROCESSING

The MATLAB code for data processing is presented below.

Listing A.1. MATLAB code

```
% ****************< CONTROL PANEL >*************************************
clear all;
clc;

path='C:\Users\Srikar\Desktop\Codes\data\';      % Data file directory path
num = 1;             % Measurement file number to access
fl = 5;               % Low frequency in GHz
fH = 9;               % High frequency in GHz
tl = 0;            % Lower limit of the time gate; in ns  {If zero, will ask for user input}
th = 0;            % Higher limit of the time gate; in ns {If zero, will ask for user input}
taper=0.5;            % Tukey window taper factor

% ********************************************************************************
% ********************************************************************************

fheader_s='s33s_';
fheader_o='s33o_';
filename_s=[path,fheader_s, num2str(num),'.dat'];
filename_o=[path,fheader_o, num2str(num),'.dat'];

A=importdata(filename_s);
fS=A(:,1)/1e9;
SS=A(:,2)+i*A(:,3);
A=importdata(filename_o);
fO=A(:,1)/1e9;
SO=A(:,2)+i*A(:,3);

[tS, RS]=f_VNA_TD(fS,SS,2^21);
[tO, RO]=f_VNA_TD(fO,SO,2^21);

t=tO;
R=RO-RS;

%Short-time Fourier Transformation
index=find(t<20);  % first 25ns of data
tA=t(index);
A=R(index);
Fs=1/(tA(2)-tA(1));
tA=[0:length(A)-1]/Fs;
WindowLen=round(length(A)/30);
WindowStep=round(WindowLen/2);
H0=figure(1);
spectrogram((A-mean(A)).',WindowLen,WindowStep,2^15,Fs);axis([fl fH 0 max(tA)]);xlabel('Frequency (GHz)'); ylabel('Time (ns)'); set(H0, 'color', 'white');
h_xlabel = get(gca,'XLabel');
set(h_xlabel,'FontSize',18);
h_xlabel = get(gca,'YLabel');
set(h_xlabel,'FontSize',18);
set(gca,'FontSize',18);
H1=figure(2); plot(tA, A); grid on; hold on;

% windowing of the signal
if (tl==0)
    tl=input('input start time: ');
end
if (th==0)
    th=input('input end time: ');
end
index=find(tA>tl & tA<th);
tc=tA(index);
Ac=A(index);
W = tukeywin(length(tc),taper);
tempo=W'.*Ac;
figure(H1);plot(tc, Ac, 'r'); xlabel('Time (ns)'); ylabel('Amplitude');
set(H1, 'color', 'white');
h_xlabel = get(gca,'XLabel');
set(h_xlabel,'FontSize',18);
h_xlabel = get(gca,'YLabel');
set(h_xlabel,'FontSize',18); %
set(gca,'FontSize',18); xlim([0 15]);

[fk, Rfft]=f_fft_fk(Ac-mean(Ac), 1/(tc(2)-tc(1)), 2^19);
rp=abs(Rfft);
rmax=max(rp);
huh=(6.5e-4)-rmax;
absRfft=rp+huh;
ff=figure(3); plot(fk, absRfft); grid on; axis([fl fH min(absRfft) (max(absRfft)+(0.25e-4))]);set(ff, 'color', 'white');
xlabel('Frequency (GHz)'); ylabel('Amplitude');
```

```
h_xlabel = get(gca,'XLabel');
set(h_xlabel,'FontSize',18);
h_xlabel = get(gca,'YLabel');
set(h_xlabel,'FontSize',18);
set(gca,'FontSize',18);
[maximum_val,resonant_position] = max(Rfft);
resonant_frequency=fk(resonant_position)*1e9
```

Listing A.2. MATLAB code

```
clear all;
clc;

numb = 10;              % Number of measurement files
fl = 5;                 % Low frequency in GHz
fH = 9;                 % High freq. in GHz
tl = 6;                 % Lower limit of the time gate; in ns  {If zero, will ask for user input}
th = 12;                % Higher limit of the time gate; in ns {If zero, will ask for user input}
path='C:\Users\Srikar\Desktop\Codes\data\';      % Data files directory path

for j=2:numb          % Ignores first data file
    arr_fr(j-1)=f_vna_dp((j-1),fl,fH,tl,th,path);
    compl=((j-1)/(numb-1))*100;
    clc;
    disp(sprintf('Processing %2.0f data files...',(numb-1)));
    disp(sprintf('Data processing %3.0f%% complete...',compl));
end

resonant_frequency=(mean(arr_fr))/(1e9);
std_deviation_frequency=(std(arr_fr))/(1e6);
disp(sprintf('Resonant frequency is %3.2f GHz.',resonant_frequency));
disp(sprintf('Standard deviation is %3.2f MHz.',std_deviation_frequency));
```

Listing A.3. MATLAB function

```
function [fr]=f_vna_dp(num,fl,fH,tl,th,path)

fheader_s='s33s_';
fheader_o='s33o_';

filename_s=[path, fheader_s, num2str(num),'.dat'];
filename_o=[path, fheader_o, num2str(num),'.dat'];

A=importdata(filename_s);
fS=A(:,1)/1e9;
SS=A(:,2)+i*A(:,3);
A=importdata(filename_o);
fO=A(:,1)/1e9;
SO=A(:,2)+i*A(:,3);

[tS, RS]=f_VNA_TD(fS,SS,2^21);
[tO, RO]=f_VNA_TD(fO,SO,2^21);

t=tS;
R=RO-RS;

%Short-time Fourier Transformation
index=find(t<20);  % first 25ns of data
tA=t(index);
A=R(index);
Fs=1/(tA(2)-tA(1));
tA=[0:length(A)-1]/Fs;

% windowing of the signal
if (tl==0)
    tl=input('input start time: ');
end
if (th==0)
    th=input('input end time: ');
end
index=find(tA>tl & tA<th); % 010509: find signal within the range
tc=tA(index);
Ac=A(index);
[fk, Rfft]=f_fft_fk(Ac-mean(Ac), 1/(tc(2)-tc(1)), 2^19);
[maximum_val,resonant_position] = max(Rfft);
fr=fk(resonant_position)*1e9;
```

Listing A.4. MATLAB function

```
function [t, R]=f_VNA_TD(f, S, Nfft)
f0=[0:f(2)-f(1):min(f)-(f(2)-f(1))].';
f=[f0;f];
S=[zeros(size(f0));S];
S=[S;zeros(Nfft-length(S),1)]; % zero pad the spectrum to Nfft number of data points
% convert the S data back to time domain
[t, R]=f_ifft_t(S, f(2)-f(1));
```

Listing A.5. MATLAB function

```
function [t, Rifft]=f_ifft_t(Rcfft, fs)
[M, N]=size(Rcfft);

if N==1
    Rcfft=Rcfft.';
end

M=2*length(Rcfft);
Rcfft=[Rcfft, 0, conj(fliplr(Rcfft))];
Rcfft=Rcfft(1:M);
Rifft=ifft(Rcfft);  % digital inverse fft
t=1/fs*[0:M-1]/M;
```

Listing A.6. MATLAB function

```
function [fk, Rfft]=f_fft_fk(R, fs, Nfft)
Rfft=fft(R, Nfft);  % fft of signal R
Rfft=Rfft(1:floor(Nfft/2));
fk=fs*[0:floor(Nfft/2)-1]/Nfft;
return
```

REFERENCES

[1] J.K. Abraham and V.K. Varadan. Modeling of passive wireless sensors for RFID tag applications. In *Proceedings of SPIE*, volume 6172, page 617204, 2006.

[2] IJ Bahl and P. Bhartia. *Microstrip antennas*. Artech House, 1980.

[3] C. A. Balanis. *Antenna theory : analysis and design*. 2005.

[4] JR Bray and L. Roy. Microwave characterization of a microstrip line using a two-port ring resonator with an improved lumped-element model. *IEEE Transactions on Microwave Theory and Techniques*, 51(5):1540–1547, 2003.

[5] J.C. Butler, A.J. Vigliotti, F.W. Verdi, and S.M. Walsh. Wireless, passive, resonant-circuit, inductively coupled, inductive strain sensor. *Sensors and Actuators A: Physical*, 102(1-2):61–66, 2002.

[6] S.B. Byun, J.A. Lee, J.H. Lim, and T.Y. Yun. Reconfigurable Ground-Slotted Patch Antenna Using PIN Diode Switching. *ETRI journal*, 29(6):832–834, 2007.

[7] K. Carver and J. Mink. Microstrip antenna technology. *IEEE Transactions on Antennas and Propagation*, 29(1):2–24, 1981.

[8] F.K. Chang. *Structural health monitoring: current status and perspectives*. CRC, 1997.

[9] K. Chang and L.H. Hsieh. *Microwave ring circuits and related structures*. Wiley-IEEE, 2004.

[10] P.C. Chang, A. Flatau, and SC Liu. Review paper: health monitoring of civil infrastructure. *Structural Health Monitoring*, 2(3):257, 2003.

[11] D. Dardari and R. DErrico. Passive Ultrawide Bandwidth RFID. *energy*, 500:3, 2008.

[12] S. Deshmukh and H. Huang. Wireless interrogation of passive antenna sensors. *Measurement Science and Technology*, 21:035201, 2010.

[13] D. Gould, M. Meiners, W. Benecke, and W. Lang. Condensation Detection Using a Wirelessly Powered RF-Temperature Sensor. *IEEE Trans. Veh. Technol.*, 58:1667–1672, 2009.

[14] MA Hamstad, A. OGallagher, and J. Gary. A wavelet transform applied to acoustic emission signals: Part 1: Source Identification. *Journal of Acoustic Emission*, 20:39–61, 2002.

[15] T.J. Harpster, B. Stark, and K. Najafi. A passive wireless integrated humidity sensor* 1. *Sensors and Actuators A: Physical*, 95(2-3):100–107, 2002.

[16] J.S. Hollis, TJ Lyon, and L. Clayton. *Microwave Antenna Measurements*. Scientific-Atlanta, 1970.

[17] S. Hu, H. Chen, CK Law, Z. Shen, L. Zhu, W. Zhang, and W. Dou. Backscattering cross section of ultrawideband antennas. *IEEE Antennas and Wireless Propagation Letters*, 6, 2007.

[18] D. Jung, Y. Woo, and C. Ha. Modified inset fed microstrip patch antenna. In *Microwave Conference, 2001. APMC 2001. 2001 Asia-Pacific*, volume 3, 2001.

[19] P. Katehi and N. Alexopoulos. On the modeling of electromagnetically coupled microstrip antennas–The printed strip dipole. *IEEE Transactions on Antennas and Propagation*, 32(11):1179–1186, 1984.

[20] S.L. Lu and AM Ferendeci. Coupling modes of a ring resonator side coupled to a microstripline. *Electronics Letters*, 30(16):1314–1315, 1994.

[21] I. Mohammad and H. Huang. Monitoring fatigue crack growth and opening using antenna sensors. *Smart Materials and Structures*, 19:055023, 2010.

[22] RP Owens. Curvature effect in microstrip ring resonators. *Electronics Letters*, 12:356, 1976.

[23] K. Penttila, M. Keskilammi, L. Sydanheimo, and M. Kivikoski. Radar cross-section analysis for passive RFID systems. *IEE Proceedings-Microwaves, Antennas and Propagation*, 153(1):103–109, 2006.

[24] JK Perng, WD Hunt, and PJ Edmonson. Development of a shear horizontal SAW RFID biosensor. *2007 IEEE Sensors*, pages 691–694, 2007.

[25] D. Pozar. Analysis of finite phased arrays of printed dipoles. *IEEE Transactions on Antennas and Propagation*, 33(10):1045–1053, 1985.

[26] DM Pozar. Microstrip antenna aperture-coupled to a microstripline. *Electronics Letters*, 21:49, 1985.

[27] K. Sarabandi and ES Li. Microstrip ring resonator for soil moisture measurements. *IEEE Transactions on Geoscience and Remote Sensing*, 35(5):1223–1231, 1997.

[28] H. Sekine, S.E. Fujimoto, T. Okabe, N. Takeda, and T. Yokobori. Structural health monitoring of cracked aircraft panels repaired with bonded patches using fiber Bragg grating sensors. *Applied Composite Materials*, 13(2):87–98, 2006.

[29] C. Sekine-Pettite. Structural Health Monitoring.

[30] M. Shigeishi, S. Colombo, KJ Broughton, H. Rutledge, AJ Batchelor, and MC Forde. Acoustic emission to assess and monitor the integrity of bridges. *Construction and building materials*, 15(1):35–49, 2001.

[31] R.A. Silva-Muñoz and R.A. Lopez-Anido. Structural health monitoring of marine composite structural joints using embedded fiber Bragg grating strain sensors. *Composite Structures*, 89(2):224–234, 2009.

[32] H. Sohn, C.R. Farrar, FM Hemez, DD Shunk, DW Stinemates, BR Nadler, et al. A review of structural health monitoring literature: 1996–2001. *Los Alamos National Laboratory, Los Alamos, NM*, 2004.

[33] Stanislav Sykor. Approximations of Ellipse Perimeters and of the Complete Elliptic Integral E(x). *url http://www.ebyte.it/library/docs/math05a/EllipsePerimeterApprox05.html*.

[34] U. Tata, H. Huang, RL Carter, and JC Chiao. Exploiting a patch antenna for strain measurements. *Measurement Science and Technology*, 20:015201, 2009.

[35] V. Volkovas and J. Dulevicius. Acoustic emission used for detection of crack generation in propellers of turbine-pump units. *Russian Journal of Nondestructive Testing*, 42(4):248–254, 2006.

[36] W. Wang, K. Lee, T. Kim, and S. Yang. Development of wireless MEMS sensor for RFID tag and temperature/pressure monitoring. In *Proceedings of SPIE*, volume 6463, page 64630Q, 2007.

[37] I. Wolff. Microstrip bandpass filter using degenerate modes of a microstrip ring resonator. *Electronics Letters*, 8:302, 1972.

[38] I. Wolff and N. Knoppik. Microstrip ring resonator and dispersion measurement on microstrip lines. *Electronics Letters*, 7:779, 1971.

[39] QS Wu, Q. Xue, and CH Chan. Bandpass filter using microstrip ring resonators. *Electronics Letters*, 39(1):62–64, 2003.

[40] L. Yu and V. Giurgiutiu. Advanced signal processing for enhanced damage detection with piezoelectric wafer active sensors. *Smart Structures and Systems*, 1(2):185–215, 2005.

BIOGRAPHICAL STATEMENT

Srikar Deshmukh was born in Bangalore, India in 1986. He completed his Bachelor's in Telecommunication Engineering from the Visvesvaraya Technological University, India in 2008. He then joined the University of Texas at Arlington to pursue his Masters in Electrical Engineering. Srikar is working as a graduate research assistant at the Advanced Sensor Technology Laboratory since October 2008. He published 3 conference papers and 2 journal papers at the time of his graduation. He also holds a provisional patent with Dr. Haiying Huang for the wireless interrogation technique. His research interest lies in microwave measurements and antenna design. He is also interested in Embedded Systems design and has a good knowledge of microprocessors. He is a licensed amateur radio hobbyist with a call sign VU3GOJ.